Predicting microstructure and strength of maraging steels: elemental optimisation

E.I. Galindo-Nava*,[1], W.M. Rainforth[2], P.E.J. Rivera-Díaz-del-Castillo[1]

[1]Department of Materials Science and Metallurgy, University of Cambridge

27 Charles Babbage Rd, Cambridge, CB3 0FS, UK

[2]Department of Materials Science and Engineering, University of Sheffield

Mappin St, Sheffield, S1 3JD, UK

*email: eg375@cam.ac.uk, +44 1223 334300

Abstract

A physics–based modelling framework to describe microstructure and mechanical properties in maraging steels is presented. It is based on prescribing the hierarchical structure of the martensitic matrix, including dislocation density, and lath and high–angle grain boundary spacing. The evolution of lath–shaped reverted austenite is described using grain–boundary diffusion laws within a lath unit. The dislocation density provides the preferential nucleation sites for precipitation, whereas descriptions for particle nucleation, growth and coarsening evolution are identified for Ni_3Ti, NiAl and its variants, and BCC–Cu clusters. These results are combined to describe the hardness at different ageing temperatures in several Fe–Ni–, Fe–Mn– and Fe–Ni–Mn–based steels. A critical assessment on individual contributions of typical alloying elements is performed. Ni and Mn control the kinetics of austenite formation, where the latter shows stronger influence on the growth kinetics. Ti additions induce higher hardness by precipitating stronger Ni_3Ti, whereas Cu clusters induce low strength. A relationship between the reverted austenite and the total elongation in overaging conditions is also found. This result allows to identify optimal process and alloy design scenarios to improve the ductility whilst preserving high hardness in commercial maraging steels.

Keywords: Martensite; Modelling; Precipitation hardening; Austenite; Intermetallics

1 Introduction

Maraging steels combine exceptional properties, including high strength and toughness, high strength to weight ratio, good weldability, simplicity of heat treatments and dimen-

sional stability. These properties stem from the complex microstructures forming during hot processing: (i) A hierarchically–arranged lath martensite matrix (α') decorated by (ii) nano–sized intermetallic precipitates and (iii) austenite laths (γ) that re–precipitate from α'. The first two items dictate mostly the hardness, whilst the partial reversion from martensite to austenite strongly influences their ductility and toughness [1, 2]. Additionally, complicated interactions between alloying elements and the evolving microstructure occur during ageing. For instance, grain–boundary embrittlement occurring in underaged conditions is due to Mn and Ni segregation to the prior–austenite boundaries, becoming ductile again during overaging [1,2]. This effect is induced by austenite reversion, promoting Ni and Mn partitioning into the γ, and by overaging grain–boundary precipitates [1].

Systematic experimental studies have been performed to explore optimal compositions for improving the mechanical properties of maraging steels [3–7], whilst optimisation algorithms have been postulated to link alloying additions with strength variations [8–10]. Although the optimisation methods show good correlation with experiments, no detailed microstructural information is predicted; this limits their application to other compositional scenarios. Additionally, thermokinetics methods have been applied to understand how the chemical composition affects intermetallic [11] and reverted austenite [12, 13] evolution; however, these approaches have not provided a direct link with mechanical properties, including strength and elongation.

These results show that, in spite of the considerable work done to improve the properties of maraging steels, a unified physics–based modelling framework is missing. Such could provide direct links between the microstructure and mechanical properties for different compositions and heat treatments. A key reason for this is the lack of a description for the martensitic matrix, as its hierarchical structure strongly controls microstructure evolution [6, 12, 14]: a high dislocation density in the laths accelerates precipitation nucleation, whereas the segregation of γ–stabilising elements into the lath boundaries determines the morphology and kinetics of the reverted austenite [14–16].

The objective of this work is to present a modelling suite for describing microstructure evolution and mechanical properties in maraging steels, including effects of chemical

composition and initial microstructure. The models are based on a previous description of the hierarchical structure of lath martensite in Fe–C steels [17, 18], where the density of dislocations, laths, and high–angle grain boundaries were prescribed in terms of the prior–austenite grain size and ageing conditions; the extension of the martensite models to maraging steels is presented in Section 3. These features will allow us to provide the microstructural landscape for modelling reverted austenite and precipitation evolution in Sections 4 and 5, respectively. These results are combined in Section 6 to link the resulting microstructure with the hardness of maraging steels. Model validation with experimental data in 19 steels is presented in Sections 7 and 8. A critical assessment on individual contributions of the typical alloying elements to the yield strength and ductility is presented in Section 8.1. A direct link between the volume fraction of reverted austenite and the total elongation in several grades is established in Section 8.2. This allows exploring optimal compositions and processing scenarios for improving the ductility whilst preserving high strength. Concluding remarks are outlined in Section 9.

2 Materials and Methods

A number of Fe–Ni–, Fe–Mn–, and Fe–Ni–Mn–based maraging steels were studied following various ageing conditions. Table 1 shows the chemical composition and denomination of the materials tested in this work; experimental results on the microstructure and hardness have been obtained from the literature. The compositional range of these materials will allow to study several microstructural features induced by different alloying elements. The effects of other substitutional elements with less than 1 wt% are ignored due to their low contribution to microstructure evolution. It is worth noting that although the carbon content in most of the steels tested is low, a significant amount of carbides could still be present; this would promote a competition between carbide and intermetallic strengthening. Nevertheless, Schintzer *et al.* [14, 19] and Leitner *et al.* [3] did not report carbide formation in PH13-8Mo for the ageing conditions employed in this work. Similarly, Zhu *et al.* [20] did not measure any carbon content in C300. Additionally, no carbide formation was reported in M350 [21], 5Mn [22], Fe12Ni6Mn [15], LeanLAl and LeanLAl [23], and the

Mar6-13 grades [7]. No carbon content in Fe8Ni8Mn was reported [24]. Coarse TiC particles were observed in Lean7Mn, Lean10Mn and Lean12Mn in as–quenched conditions, having volume fraction of 0.22 % and a mean size of 500 nm; nevertheless, Qian [25] concluded that they have no influence on hardening due to their size. Similarly, carbide formation in 17-4 SS has been reported [26]; Viswanathan *et al.* [27] have explored their effects in strengthening, concluding that it is low. Carbide formation in AISI 301 has been reported, however only reverted austenite kinetics is explored in this work. These results show that, for the conditions tested in this work, carbide contribution to strengthening can be ignored. Additionally, except for C300, only Co–free steels are considered in this study, as this work is focused on cost–efficient alloy development. Similarly, it will be assumed that the martensite laths are fully formed in as–quenched conditions and no retained austenite is present, unless otherwise stated; this is to consider a homogenous structure during ageing.

3 Martensite structure

The microstructure of lath martensite in Fe–C steels has been described in previous work [17, 18]. The martensite matrix consists of fine lath units (∼100–300 nm thick) hierarchically arranged in substructures within the prior–austenite grains (PAG), namely packets and blocks of individual laths. These arrangements accommodate the crystallographic distortions during the transformation from austenite into martensite and ensuring that the net strain in the prior austenite grain is pure dilatation [28]. The packet (d_{packet}) and block (d_{block}) sizes are proportional to the prior–austenite grain size (D_g), where the proportionality constants are determined by the variant number of the austenite/martensite transformation habit planes within an austenite grain and the crystallographic orientation of the laths within a packet, respectively [17]:

$$\begin{aligned} d_{packet} &= \sqrt{\frac{3\sqrt{3}}{8N_p}}D_g = \sqrt{\frac{3\sqrt{3}}{32}}D_g = 0.40D_g, \\ d_{block} &= \frac{1}{N_b}d_{packet} = \frac{1}{6}d_{packet} = 0.067D_g, \end{aligned} \tag{1}$$

where $N_p = 4$ and $N_b = 6$ are the number of packets in a PAG and number of

blocks in a packet, respectively [29, 30]. This has also been validated in a Fe-9Ni (wt%) martensite [28]. Figure 1(a) shows a schematic representation of the hierarchical structure of lath martensite; laths are the fundamental unit of thickness d_{lath} and length d_{block}.

Lath boundary spacing is arranged in such form that it ensures complete relaxation of the crystallographic distortions during the phase transformation with the overall strain being pure dilatation [17, 28]. This mechanism is controlled by dislocations forming in the laths in order to conceal the local distortions produced by impurity atoms [31]. This implies that the dislocation and lattice strain energy in a lath should be equal. If the lath boundaries are formed by dislocation loops and they are assumed of cuboidal shape (Figure 1(a)), the energy per unit volume required to nucleate an interfacial dislocation of length $4d_{lath}$ (lath boundary perimeter) is given by [32] $E_{disl} = \frac{1}{2}\mu b\rho(4d_{lath})/4$, where ρ is the lath dislocation density, b=0.286 nm is the magnitude of the Burgers vector, μ=80 GPa is the shear modulus and the 1/4 factor accounts for the shared dislocation density on adjacent lath boundaries. On the other hand, the lattice strain energy produced during the phase transformation is estimated by the Stibitz equation [17, 33]: $E_{lattice} = \frac{3E\varepsilon^2}{2(1+\nu^2)}\frac{A_{lath}}{A_{random}}$, where E=211 GPa is the Young's modulus, ν=0.3 is the Poisson ratio, $\varepsilon = 0.245$ is the Bain strain [17, 34], and the $\frac{A_{lath}}{A_{random}}$ ratio accounts for the localised distortions accommodated in the lath boundary area ($A_{lath} = w_{lath}d_{lath}$, where w_{lath} is the thickness of a lath boundary), from an equivalent undistorted area in the prior–austenite phase ($A_{random} = d_{lath}^2$) [17]. For the case of Fe–C steels, w_{lath} was found equal to the length of a Cottrell atmosphere inducing carbon segregation at the lath boundaries [35]; for the case of maraging steels, we consider that w_{lath} equals the thickness of a dislocation distortion field and it has been experimentally estimated in Fe–9Mn (at%) to be $w_{lath} \approx 4$ nm [36]. Combining these results, ρ equals:

$$\rho = \frac{3E}{(1+2\nu^2)\mu}\frac{4\varepsilon^2 w_{lath}}{d_{lath}^2 b}. \tag{2}$$

d_{lath} depends on the composition of the steel and it is related to the redistribution of alloying elements into the lath boundaries. For the case of Fe–C martensite, d_{lath} was obtained by estimating the amount of carbon segregating to the lath boundaries in the form of Cottrell atmospheres [17]. Similarly, substitutional atom segregation to the lath

boundaries and dislocations occurs in Fe–Ni–Mn martensite during ageing [2,36–38], and these features could affect the values of d_{lath} with alloying content. However, small variations in d_{lath} have been observed in a variety of maraging steels with different Ni and Mn content, even for tempered conditions [14, 20, 25, 26, 39]; this behaviour can be due to the relatively low lattice distortion and high solubility of substitutional atoms in Fe with respect to C atoms; hence, based on these experimental results, it is considered that $d_{lath} = 250$ nm remains constant for all steels tested. For this case, $\rho \approx 3.6 \times 10^{14}$ m^{-2}, being this prediction consistent with experimental estimations in a stainless maraging steel [40]. The description of the grain boundary density of lath martensite in this section will allow us to describe the growth of γ in terms of the α' structure.

4 Reverted austenite kinetics

Reverted austenite nucleates at the lath and PAG boundaries [41], and growth is diffusion–controlled at a given ageing temperature [12, 14]. Moszner *et al.* [42] have suggested that austenite formation in Fe-Mn martensite follows the partitioning of Mn into the austenite nuclei, and the growth mechanisms are interface–controlled. This process is consistent with experimental evidence showing that γ–stabilising elements partition into the lath boundaries [37]. Moreover, the growth of reverted austenite is controlled by the matrix as individual nuclei will grow around the α' laths [14].

Based on the previous results, the following mechanism for austenite evolution during ageing is proposed: γ nuclei form at the lath boundaries, where they grow into the lath interiors upon eventually transforming the α' laths into γ. The thickness (r_γ) and length (L_γ) of the austenite are restricted to occupy the α' lath size (d_{lath}) and length (d_{block}), respectively. Figure 1(b) shows a schematic representation of this process in a number of laths within a block (Figure 1(a)). This mechanism is valid if the equilibrium volume fraction is high enough to fully transform the α' laths into austenite; however, if the equilibrium volume fraction of γ ($f_{\gamma,eq}$) at a given ageing temperature is lower, then r_γ and L_γ are lower than d_{lath} and d_{block} by a factor of $f_{\gamma,eq}^{1/3}$, respectively [25]; this is to account for the growth restriction effect on each direction of the austenite laths. Since

the phase transformation is interface–controlled, the thickness and length evolution of γ can be prescribed by standard grain boundary kinetics equations [43]:

$$\begin{aligned} \frac{dr_\gamma}{dt} &= M\left(\frac{\Gamma_\gamma}{r_\gamma} - \frac{\Gamma_\gamma}{d_{lath} f_{\gamma,eq}^{1/3}}\right) \\ \frac{dL_\gamma}{dt} &= M\frac{2d_{block}}{d_{lath}}\left(\frac{\Gamma_\gamma}{L_\gamma} - \frac{\Gamma_\gamma}{d_{block} f_{\gamma,eq}^{1/3}}\right), \end{aligned} \tag{3}$$

where Γ_γ is the interfacial energy between austenite and ferrite, M is the grain boundary mobility, and the $2d_{block}/d_{lath}$ term in $\frac{dL_\gamma}{dt}$ accounts for shape effects in particle growth [44]; the last term in both equations accounts for the growth restriction within the lath boundaries, where L_γ includes effects of γ formation at the PAGBs via d_{block}. The mobility is dictated by grain boundary diffusion [43]:

$$M = \frac{b_{\alpha'}^2}{k_B T} D_{\alpha',\gamma}, \tag{4}$$

where $D_{\alpha',\gamma}$ is the effective diffusion coefficient driving the $\alpha' \rightarrow \gamma$ transformation and $b_{\alpha'}$ is the lattice parameter of α' and it is considered equal to 0.286 nm. The solution to equations 3 provides the evolution of an austenite unit within a single lath; the initial nucleus size is assumed to be $b_{\alpha'}$. The volume fraction of γ is given by the ratio between the volume of transforming austenite ($r_\gamma^2 L_\gamma$) and the volume of an α' lath:

$$f_\gamma = \frac{r_\gamma^2 L_\gamma}{d_{lath}^2 d_{block}}. \tag{5}$$

This equation provides a direct link between the size of the reverted austenite and its volume fraction without the need of additional parameters. It is interesting that when $\frac{dr_\gamma}{dt} = \frac{dL_\gamma}{dt} = 0$ in equation 3, the steady state values of r_γ and L_γ equal $d_{lath} f_{\gamma,eq}^{1/3}$ and $d_{block} f_{\gamma,eq}^{1/3}$, respectively; this shows that $f_\gamma = \frac{r_\gamma^2 L_\gamma}{d_{lath}^2 d_{block}} = f_{\gamma,eq}$ reaching its equilibrium volume fraction during steady state.

For the steels tested in this work, γ is controlled by additions of Ni, Mn and Cr which are combined with Fe to increase the volume fraction of austenite at a given ageing temperature. For the case of Al, Cu and Ti additions, it has been reported that their content in the reverted austenite is significantly lower, as they mainly partition to intermetallics forming before (underaging) than γ (overaging). For instance, Schnitzer *et al.* [11] have reported in PH13-8Mo that the chemical composition in austenite is mainly composed by

Fe, Ni and Cr, whereas Al content in the γ is less than 1 at%. Similarly, in the Mar6–13 series (Fe-Ni-Mn-Al-Cu steels), Kapoor *et al.* [7] reported that most of the Al and Cu atoms partition to the intermetallics, although no reverted austenite composition was reported for the conditions tested. As for molybdenum, it remains mostly in solid solution in α' during underaging, and later forming Mo–rich intermetallics during overageing [45, 46]. These results allow us simplifying the description for $D_{\alpha',\gamma}$ by approximating it to an effective interdiffusion between α' and γ of Fe, Ni, Mn and Cr [47]:

$$D_{\alpha',\gamma} = \frac{1}{\frac{(x_{Fe,\gamma}-x_{Fe,\alpha'})^2}{x_{Fe,\alpha'}D_{Fe}} + \frac{(x_{Ni,\gamma}-x_{Ni,\alpha'})^2}{x_{Ni,\alpha'}D_{Ni}} + \frac{(x_{Mn,\gamma}-x_{Mn,\alpha'})^2}{x_{Mn,\alpha'}D_{Mn}} + \frac{(x_{cr,\gamma}-x_{Cr,\alpha'})^2}{x_{Cr,\alpha'}D_{Cr}}} \quad (6)$$

where $x_{Fe,i}$, $x_{Ni,i}$, $x_{Mn,i}$ and $x_{Cr,i}$ are the equilibrium concentrations of Fe, Ni, Mn and Cr in each phase ($i = \alpha', \gamma$), respectively, and D_{Fe}, D_{Ni}, D_{Mn} and D_{Cr} are the diffusion coefficients of Fe, Ni, Mn and Cr in $\alpha'-$Fe, respectively. $x_{Fe,i}$, $x_{Ni,i}$, $x_{Mn,i}$ and $x_{Cr,i}$ values can be obtained using the CALPHAD software Thermocalc for a given composition and temperature, whereas the diffusion coefficient values are shown in Table 3, with $D_i = D_0 \exp\left(-\frac{Q}{R_g T}\right)$. Diffusion parameters in ferrite are considered in this work due to the lack of information on interdiffusion in martensite. For the case of the interfacial energy, Rajasekhara and Ferreira [12] have found in AISI 301LN (Fe-6.5Ni-1.29Mn wt%) $\Gamma_\gamma = 1.3$ J/m^2. Similar values ($\sim$1 J/m^2) have also been reported for phase–field simulations on austenite to ferrite transformation [48, 49]. However, Lange *et al.* [50] employed lower values (0.5–0.6 J/m^2) to describe austenite$\rightarrow$ferrite transformation kinetics in Fe–C steels. In all cases, Γ_γ strongly depends on chemical composition. For instance, Qian [25] has found experimentally that the kinetics of γ increase with increasing Mn content; similarly, austenite reversion occurs faster in steels with high Ni additions (18 wt%) [51], than for steels with lower Ni content (8.2 wt%) [14]. An empirical formula for the interfacial energy was obtained by adjusting it to the experimental data of the steels tested in this work: $\Gamma_\gamma = 0.25 \exp(7x_{Mn,\gamma} + 4x_{Ni,\gamma})$ J/m^2; using this formula Γ_γ in AISI 301LN is estimated to be 0.62 J/m^2. The description of austenite kinetics in terms of chemical composition and ageing conditions will allow relating these features to the total elongation in Section 8.

5 Precipitation kinetics

5.1 Compositional effects on intermetallic formation

Understanding the role of each alloying element in the structure of the formed intermetallics is key to elucidate their relative contribution to mechanical properties. Table 2 shows typical intermetallics observed, as well as their morphologies, within different compositional ranges of multicomponent Co–free maraging steels for ageing temperatures in the range 450–600 °C*; the constituents of each multicomponent system are marked by an X. Cobalt was included in the initial developments of maraging steels as it reduces the solubility of Mo increasing the fraction of Ni_3(Ti,Mo) [6] and promoting the precipitation of Fe_2Mo (laves phase) [52]. However, the effect of cobalt on the mechanical properties can be compensated by increasing the content of Ti [5, 6].

Nickel is one of the most important elements in maraging steels, as it is not only a γ–stabiliser element, but also the main constituent of several intermetallics forming in these steels. Similarly, Mn is a γ–stabiliser element and can influence the content and structure of the forming intermetallics. For the ternary Fe-Ni-Mn system, ordered face–centred tetragonal NiMn (θ) particles of lenticular shape form; Heo *et al.* [16] have reported that they transform into austenite after long ageing periods. He & Lee [24] observed that Al additions in Fe-Ni-Mn promote the transition from θ to finely dispersed Ni_2MnAl; this effect also increases the strength of the steel [23]. Schober *et al.* [53] observed in Fe-Ni-Al-Mo the formation of β'-NiAl†. Small additions of Ti partition into NiAl forming Ni_2AlTi in Fe-Ni-Mn-Al-Ti when nickel content is low ($\leq$ 4 wt%) [4, 25, 54], whilst very low amounts of Mn atoms partition into the precipitates. No Mo partitioning to NiAl and its variants in Al–containing steels has been observed [23, 25]. This shows that Ni and Al have strong interrelations as they tend to form B2 intermetallics; Ti and Mn additions modify this structure by transitioning into $L2_1$ precipitates, and when both elements are added, Ti has preference to form Ni_2AlTi.

Ti additions to the Fe-Ni-Ti-Mo system promote the formation of rod–shaped Ni_3Ti (η)

*Although BCC-Cu is not an intermetallic phase, the same evolution descriptions will be adopted for all precipitates. Hence, to simplify the notations they will also be referred to as intermetallics.

†Although this alloy contained 0.39 wt% of Mn, it was not enough to form θ intermetallics.

in high–Ni containing steels, showing an apparent higher strength than the Al–containing steels at lower ageing temperatures [23,25]. Mo additions to this system in Co–free alloys promote the formation of the laves phase Fe_2Mo; however, Tewari *et al.* [45] showed that Fe_2Mo intermetallics form at temperatures below 500 °C and after 100 hours of ageing due to the low diffusivity of Mo in Fe. Hence, they concluded that only the η particles contribute to the peak hardness in Fe-18Ni-Ti-Mo (wt%). Although it has been suggested that Mo contributes to the formation of Ni_3(Ti,Mo) in Co–free alloys [55], experimental evidence shows that only small amounts of Mo partition into η [52]; moreover, similar peak hardnesses have been measured in Fe-18Ni-2.6Ti-Mo (wt%) containing different Mo contents [56], indicating no increase in the η volume fraction. Additions of Mn up to 3.5 wt% do not modify the structure of Ni_3Ti [57].

When increasing the number of alloying elements, Leitner *et al.* [58] found in the Fe-Ni-Al-Ti-Mo-Cr system that both Ni_3(Ti,Al) and NiAl particles form simultaneously; however, Ni_3(Ti,Al) nucleation was only possible due to the higher Ni content in the alloy (9 wt%). Moreover, when Cu is added to the Fe-Cr-Ni-Al-Ti-Cu system, Schnitzer *et al.* [19] have found that Ni_3(Ti,Al) forms at the interface between the matrix and Cu clusters. BCC-Cu precipitates evolve to a twinned 9R structure until they ultimately transform to an equilibrium FCC structure after long ageing times [59]. Similarly, Kapoor *et al.* [7] have shown that the yield strength can increase up to 1.6 GPa in Fe-Ni-Mn-Al-Cu by systematically increasing Cu and Al content to precipitate Cu clusters and Ni_2AlMn.

In summary, there are four intermetallic systems for study in the typical compositional range of maraging steels: 1) NiMn forms in the Fe-Ni-Mn system. 2) NiAl and variants form when adding Al in Fe-Ni-Al, Fe-Ni-Mn-Al and Fe-Ni-Mn-Al-Ti. 3) Ni_3Ti forms by Ti additions in Fe-Ni-Ti and in Fe-Ni-Ti-Al if Ni content is high enough. 4) Cu additions promote the formation of BCC clusters that will form independently from other intermetallics. These results allow us to describe precipitation behaviour on each particle system and determine their individual contribution to the hardness for each alloy tested.

5.2 Modelling precipitation kinetics

A mean radius approach is adopted for describing the evolution of each intermetallic species. This includes employing classical nucleation theory to estimate the nucleation rate and Zener's law to describe growth kinetics [60,61]. Additionally, since grain boundary embrittlement occurs during underaging, the analysis is focused on precipitation behaviour in the vicinity of the peak hardness and during overaging, hence classical coarsening laws are also included.

Multiple species of precipitates are considered, including single (Cu) and multicomponent systems with 2 (NiAl, NiMn, Ni_3Ti) and 3 (Ni_2AlTi, Ni_2AlMn) constituents. In order to use the same formalism for all intermetallics and simplify the analysis, modelling of single–component precipitation is assumed, where the constituent with the slowest diffusivity in Fe controls the evolution kinetics [62], *i.e.* the diffusion coefficient (D_p) during nucleation, growth and coarsening equals the diffusion coefficient of the constituent j holding the lowest $\frac{D_j}{x_{j,p}}$ ratio [63], where $x_{j,p}$ is the equilibrium concentration in the intermetallic p and D_j is the diffusion coefficient of j element in Fe. For instance in NiAl, $x_{Ni,p} = x_{Al,p} = 0.5$, and in Ni_3Ti, $x_{Ni,p} = 0.75$ and $x_{Ti,p} = 0.25$. Table 3 shows the diffusion parameters of the relevant constituents showing that, for the range of temperatures tested (400-575 °C), the diffusion coefficient of Ni controls the kinetics of NiMn, Ni_3Ti, NiAl, Ni_2AlMn and Ni_2AlTi. This simplification has been applied to multicomponent particles in Ni– and Fe–based alloys [62–64].

The nucleation rate of new particles is given by [60]:

$$J_p = \frac{dN_p}{dt} = N_0 Z \beta^* \exp\left(- \frac{4\pi\gamma_p (r_p^*)^2}{3k_B T} \right) \exp\left(- \frac{\tau}{t} \right), \tag{7}$$

where N_0 are the potential nucleation sites for precipitation, $Z = \frac{V_m}{2\pi r_p^*}\sqrt{\frac{\gamma_p}{k_B T}}$, $\beta^* = \frac{4\pi r_p^* D_p x_{j,\alpha'}}{a^4}$ and $\tau = \frac{2}{\pi\beta^* Z^2}$ are constants dictated by the particle's molar volume V_m, critical radius for nucleation r_p^*, interfacial energy γ_p and instantaneous concentration of the constituent j in the matrix towards forming the precipitates $x_{j,\alpha'}$. In maraging steels, dislocations are ideal sites for precipitation nucleation due their high density [65] [‡]. Hence, the number of nucleation sites (m^{-3}) for precipitation is given by [44]: $N_0 = \frac{\rho}{b}$.

[‡] ρ also includes possible precipitation around lath boundaries (Section 3).

The critical radius dictates the minimum size to reach the critical energy for nucleation and it is given by [61]:

$$r_p^* = \frac{2\gamma_p V_m}{R_g T \ln\left(\frac{x_{j,\alpha'}}{K_{eq}}\right)}, \tag{8}$$

where K_{eq} is a constant related to the solubility product of $x_{j,\alpha'}$ in the matrix with respect to the intermetallic phase (p) [61].

Particle growth is given by Zener's law [61]:

$$\frac{dr_p}{dt}|_{growth} = \frac{D_p}{r_p}\frac{x_{j,\alpha'} - x_{j,int}}{x_{j,p} - x_{j,int}}, \tag{9}$$

where $x_{j,int}$ is the concentration of element j at the matrix/particle interface and it is given by the Gibbs–Thomson relation [66]:

$$x_{j,int} = K_{eq} \exp\left(\frac{2\gamma_p V_m}{r_p R_g T}\right). \tag{10}$$

$x_{j,\alpha'}$ represents the effective concentration of j in α' diffusing towards forming p; however, the equilibrium volume fraction of p is limited by the constituent with the lowest concentration (x_0) diffusing to the particle. For instance, the volume fraction of NiAl in Fe-8Ni-2Al (at%) is limited by Al (although Ni is controlling elemental interdiffusion), as there are less Al atoms available to form the intermetallic phase [11]; this implies that $0 \leq x_{j,\alpha'} \leq x_0$, with $x_0 = 2$ at% being the initial value for $x_{j,\alpha'}$. For Ni_3Ti, x_0 can be obtained using the CALPHAD software Thermocalc, by estimating the effective concentration of Ti diffusing to the particle: $x_0 = x_{Ti,p} f_{p,eq} = 0.25 f_{p,eq}$, where $f_{p,eq}$ is the predicted equilibrium volume fraction of Ni_3Ti at a given composition and ageing temperature. However, for NiMn, NiAl, Ni_2AlMn, Ni_2AlTi, and Cu, these phases are not predicted in the equilibrium phase diagrams of the respective systems, as some of these phases are metastable [16, 59]. Nevertheless, x_0 can be computed by using the lever rule [67]. For instance, in NiMn, $x_0 = \min(x_{Ni}, x_{Mn})$, where the min function limits the increase in the particle fraction by the constituent with minimum content; similarly for Ni_2TiAl, it gives $x_0 = \min(x_{Ni}, (x_{Al} + \min(x_{Al}, x_{Mn})))$; the second min function is to

account for gradual transition from B2 to $L2_1$ [68].

The particle number density (N_p) and radius (r_p) are obtained by combining equations 7, 9 and 10, where K_{eq} is the only fitting parameter. The volume fraction is then given by:

$$f_p = \frac{4\pi r_p^3}{3x_{j,p}} N_p, \tag{11}$$

where the $x_{j,p}^{-1}$ term accounts for the effective increment in the volume fraction when the constituent j diffuses to p in a multicomponent intermetallic [60].

As particles form, the content of each constituent (j) in the matrix decreases until reaching an equilibrium concentration according to:

$$x_{j,\alpha'} = \frac{x_j - x_{j,p} f_p}{(1 - f_p)}, \tag{12}$$

where x_j is the atom fraction of element j in the steel.

Large particles coarse at the expense of the smaller ones and equation 8 dictates that particles with size below r_p^* are unstable, undergoing dissolution. Thus, since r_p^* increases during growth, the transition from particle growth to coarsening occurs when the equilibrium volume fraction is reached and $r_p^* = r_p$. The mean radius during coarsening is given by:

$$r_p = \left(r_0^3 + k_p t\right)^{1/3}, \tag{13}$$

where r_0 is the initial radius in the coarsening step and k_p is given by [44]:

$$k_p = \frac{8\gamma_p V_m D_p x_{j,p}}{9 R_g T}. \tag{14}$$

Once the phase fraction reaches equilibrium, the particle number density decreases due to coarsening (overaging), according to the relation [69]: $N_p = \frac{3 f_p x_{j,p}}{4\pi r_p^3}$. It is worth noting that additional expressions have been proposed to account for a "smooth" transition[§] between growth and coarsening [60,70]. These are usually fitted in the form of exponential decay or power laws of the ratio between r_p^* and r_p. However, they require introducing a number of fitting parameters, thus they are not included in the models to simplify the descriptions.

For the non–spherical intermetallics tested (NiMn and Ni_3Ti), the average aspect ratio (a_r) between their length (l_p) and diameter ($2r_p$) has been measured to be almost constant: a_r for Ni_3Ti has been found to be ≈ 4.5 [20], whereas for NiMn a_r is approximately 3 [71].

[§]Since the growth and coarsening equations in 9 and 13 evolve according to $\sim t^{1/2}$ and $\sim t^{1/3}$, respectively, a sharp variation in r_p can be observed at the transition when $r_p^* \approx r_p$.

Hence, the relation $l_p = 2a_r r_p$ is adopted. Additionally, the particle volume in equation 11 is modified to include this effect in f_p and N_p, becoming $f_p = N_p \frac{2a_r \pi r_p^3}{x_{j,p}}$ and $N_p = \frac{f_p x_{j,p}}{2a_r \pi r_p^3}$ (during coarsening).

The required parameters for each intermetallic are $f_{p,eq}$, γ_p and K_{eq}; the latter is fitted equal to $K_{eq} = 0.0001$ in all cases. As for the interfacial energy in NiMn, it is assumed to be $\gamma_{NiMn} = 0.2$ J m^{-2}. For NiAl, γ_p has been estimated to be 0.02 J m^{-2} in Fe–Ni–Al–Mo [72]; however, the kinetics of NiAl and variants increase with Mn content [25]; hence, based on the effect of Mn in NiMn and austenite reversion, the factor $\exp(7x_{Mn})$ is added to the interfacial energy: $\gamma_{NiAl} = 0.02 \exp(7x_{Mn})$ J m^{-2}; For Ni_2AlMn and Ni_2AlTi, the interfacial energy is assumed to be $\gamma_{Ni2AlMn} = \gamma_{Ni2AlTi} = 0.1 \exp(7x_{Mn})$ J m^{-2}. The interfacial energy of Ni_3Ti is estimated to be [20]: $\gamma_{Ni3Ti} = 0.2$ J m^{-2}. For Cu clusters multiple γ_{Cu} values have been proposed [65,73]; $\gamma_{Cu} = 0.02$ m^{-2} is considered in this work. The molar volumes of NiMn, NiAl and variants, Ni_3Ti and Cu are 7.3×10^{-6} m^3/mol [74], 10^{-6} m^3/mol [75], 9×10^{-6} m^3/mol [20] and 7×10^{-6} m^3/mol [75], respectively.

These results provide descriptions with a direct link between the microstructure evolving during ageing and chemical composition. This will allow us to integrate microstructure–based models for yield stress in different steels.

6 Strengthening mechanisms in maraging steels

The yield strength of maraging steels accounts for three contributions [17]: 1) the strength of lath martensite σ_{Mart}, 2) precipitation hardening of a number of intermetallics σ_p and 3) solid solution hardening σ_{ss}. It is assumed that the reverted austenite has no effect in the strength of the steels [18]. This is is expressed in terms of the Vickers hardness as:

$$H_v = \frac{1}{3}\sigma_Y = \frac{1}{3}\big(\sigma_{Mart} + \sigma_p + \sigma_{ss}\big). \tag{15}$$

The strength of the martensitic matrix is controlled by the increase in grain boundary area and dislocation density. The block size is considered as the "effective" grain size and grain boundary strengthening is expressed in terms of a Hall–Petch equation for d_{block} [17,76], whereas the Taylor equation accounts for the strengthening contribution of the increase in the dislocation density. σ_{Mart} equals [17]:

$$\sigma_{Mart} = \frac{300}{\sqrt{d_{block}}} + 0.25 M \mu b \sqrt{\rho}, \tag{16}$$

where $M = 2.5$ is the Taylor orientation factor.

Schnitzer *et al.* [77] have tested in PH 13-8 Mo a number of models describing dislocations–particle interactions, including particle shearing (Friedel formula), Orowan bypassing and a pile–up model proposed by Ansell and Lenel [78]. The latter is based on the assumption that yielding occurs when a critical number of dislocations pile–up reaching the threshold stress to plastically deform the particles. Only the Orowan and pile–up models were able to reproduce the experimental trends for underaging, peak hardness and overaging. However, experimental observations in other materials with intermetallics of similar crystal structures do not report traces of dislocation pile–up at the particle's interface nor anti–phase boundary formation [79]. Since Friedel formula and the Orowan equation hold similar values for underaged conditions [77], it will be assumed that σ_p is dictated by the Orowan equation to simplify the analysis:

$$\sigma_p = 0.1 \mu b \frac{f_p^{1/2}}{r_p} \ln\left(\frac{r_p}{b}\right). \tag{17}$$

This equation is valid for spherical particles where $2r_p$ represents the extent of particle bypass; however, Ni_3Ti and NiMn have rod–like shape with constant aspect ratio (a) between its length l_p and thickness ($2r_p$); this morphology can increase the applied stress for dislocations to bypass particles, as they will have to cover an additional area; this is dictated by the relative orientation between the slip direction and particle alignment. Nevertheless, an equivalent circular particle of same area can be defined with radius $\rho_p = \sqrt{\frac{r_p l_p}{\pi}}$. Thus, the ratio ρ_p / r_p dictates an effective increase of the bypass length without identifying specific alignments between the particle and a dislocation, and the applied stress for dislocations to bypass rod–shaped particles can be assumed to increase according to this ratio: $\sigma_p = \frac{\rho_p}{r_p}\sigma_{p,circ} = \sqrt{\frac{a}{\pi}} 0.1 \mu b \frac{f_p^{1/2}}{r_p} \ln\left(\frac{r_p}{b}\right)$.

Ardell [80] has shown that when multiple species of precipitates are present, the total particle strengthening is given by the superposition of their individual contributions:

$$\sigma_p = \left(\sum_j \sigma_j^2 \right)^{1/2}, \tag{18}$$

where σ_j is the strength increase by an intermetallic j with volume fraction and radius

f_j and r_j, respectively (equation 17). This equation is also consistent with the lower strengthening effect produced when distinct precipitates form at the interface of other intermetallics [7], as their individual contribution is lower than if they form separately.

Solid solution strengthening is obtained with Fleischer's equation estimating the increment in the critical resolved–shear stress due to the presence of substitutional solute atoms [81, 82]: $\sigma_{ss} = \sum_i (\beta_i^2 x_{i,\alpha'})^{1/2}$, where $x_{i,\alpha'}$ is the atom fraction of substitutional element i in the matrix and β_i is the strengthening constant related to the lattice and modulus mistift of element i with respect to iron. β_i values have been obtained in previous work [17, 81], and are shown in Table 4. Ti and Mo induce the highest solid solution strengthening effect, whereas Al, Cu and Mn have the lowest contributions. The solid solution hardening effects of the particle–forming elements (Ni, Al, Mn, Ti, Cu) decreases as the volume fraction of the particles increases; this transition is obtained by a mass balance equation, where the solute content in α' is: $x_{i,\alpha'} = \frac{x_i - \sum_j x_{i,j} f_j}{1 - \sum_j f_j}$, where f_j is the volume fraction of particle j and $x_{i,i}$ its the equilibrium concentration of element i in j.

For a prior–austenite grain size of 20 μm, $\sigma_{Mart} = 450$ MPa, whereas for the alloys tested, σ_{ss} values range between 300 and 500 MPa. This gives the initial hardness to be in the range 250–330 H_v, being these predictions in agreement with experimental estimations for the hardness in as–quenched conditions [3, 20, 25, 26].

7 Results

The model results on the hardness at room temperature, reverted austenite and intermetallic evolution are tested against experimental measurements in several maraging steels (Table 1). This is done by solving equations 3, 5, 9, 11, 13 and 15 for a given composition and ageing temperature. An initial particle radius of $r_0 = 0.285$ nm is assumed in all cases. The input parameters of the models are the nominal composition, ageing temperature, and prior–austenite grain size. MATLAB scripts with the solution of all models are included as supplementary material. Results on reverted austenite evolution are tested first to show how Ni and Mn affect microstructure evolution.

Figure 2 shows the model predictions and experimental measurements of the reverted

austenite evolution with time at different ageing temperatures in PH13-8Mo, including (a) volume fraction, (b) thickness and (c) length. $D_g = 25$ μm was measured, whereas measurements report $f_{\gamma,eq} = 0.2$ and 0.3 at 525 °C [3] and 575 °C [14], respectively, $x_{Ni,\gamma} = 0.17$, $x_{Ni,\alpha} = 0.045$, $x_{Cr,\gamma} = 0.12$, $x_{Cr,\alpha} = 0.14$[¶]. The model shows good agreement with experiments in all cases. f_γ and r_γ in 5Mn aged at 650 °C are also shown in (a) and (b), respectively; for this case, D_g was assumed to be 20 μm as this value was not reported, and $f_{\gamma,eq} = 0.33$, $x_{Mn,\gamma} = 0.098$, $x_{Mn,\alpha} = 0.001$, $x_{Ni,\gamma} = 0.00626$ and $x_{Ni,\alpha} = 0.001$ were estimated using Thermocalc; the model predicts a higher volume fraction in 5Mn, however the γ size is close to the experimental values; the discrepancies can be due to higher volume fraction predicted in Thermocalc, as equilibrium has been reached for this condition. Figure 2(d) shows additional results in the $\alpha' \rightarrow \gamma$ transformation at high temperatures of cold–rolled AISI 301 and reverted austenite kinetics of M350. The lath thickness of AISI 301 was reported to be 170 nm [83], and $d_{block} = 170$ nm was considered due to the heavily deformed structure; $f_{\gamma,eq} = 1$ for all temperatures tested. For M350 an initial 5% of retained austenite is assumed, whereas $f_{\gamma,eq} = 0.64$, $x_{Ni,\gamma} = 0.24$ and $x_{Ni,\alpha} = 0.042$ were estimated using Thermocalc; $D_g = 20$ μm was assumed, as this value was not reported. The model also shows very good agreement in both steels. These results indicate that equations 3 and 5 successfully describe $\alpha' \rightarrow \gamma$ transformation kinetics for Fe–Ni– and Fe–Mn–based steels.

Figure 3 shows the combined effects of Ni and Mn on the kinetics of reverted austenite in Lean10Mn and Lean12Mn, including (a) volume fraction, thickness at (b) 500 °C and (c) at various temperatures. The prior–austenite grain size is 30 μm [25]. The parameters for (a) and (b) in Lean10Mn are (Thermocalc) $f_{\gamma,eq} = 0.33$, $x_{Ni,\gamma} = 0.05$, $x_{Mn,\gamma} = 0.25$, $x_{Ni,\alpha} = 0.001$ and $x_{Mn,\alpha} = 0.03$, whereas for Lean12Mn $f_{\gamma,eq} = 0.41$; elemental partitioning is approximately constant for all conditions. In (c), $f_\gamma = 0.35$ and 0.5 at 460 °C and 540 °C, respectively. The model underpredicts the growth rate in Lean10Mn; the discrepancies can be due to a stronger effect of Mn additions in the Γ_γ. Nevertheless, these results show that additions of Mn in the steels not only increase the volume fraction

[¶]Elemental partitioning in α is subtracted from Thermocalc and it is assumed equal than in α'.

of reverted austenite, but they can also accelerate γ growth at a given temperature. Additionally, Figure 3(d) shows f_γ results in 12Ni6Mn, where higher austenite fraction is measured at lower times; these discrepancies can be due to the presence of retained austenite in the steel, however this was not confirmed experimentally; additionally for 12Ni6Mn aged during the first 10 hours, the X-ray measurements of γ reported in [15] can also be due to the formation NiMn (fct) precipitates (Figure 3(d)), hence increasing the apparent values of f_γ during underaging. The parameters for 12Ni6Mn are $f_\gamma = 0.37$ and 0.45 at 500 °C and 538°C, respectively, whereas $x_{Ni,\gamma} = 0.25$, $x_{Mn,\gamma} = 0.15$, $x_{Ni,\alpha} = 0.02$ and $x_{Mn,alpha} = 0.001$ at 500 °C and $x_{Ni,\gamma} = 0.22$, $x_{Mn,\gamma} = 0.12$, $x_{Ni,\alpha} = 0.02$ and $x_{Mn,\alpha} = 0.001$ at 538 °C. $D_g = 20$ μm was assumed in both cases as these values were not reported.

To explore the role of Al and Mn additions on intermetallic behaviour, Figure 4 shows the model predictions in PH13-8Mo containing NiAl intermetallics and their comparison with experimental data for (a), (b) precipitation and (c) hardness evolution; the Al content of this steel at 525 °C and 575 °C is 2 and 1.5 wt%, respectively [3, 19]. $D_g = 25$ μm was considered [19]. The initial hardness is given by the martensite strength (σ_{Mart}) and solid solution hardening (σ_{ss}). The model shows very good results in almost all cases, confirming good correlation between the hardness and the predicted kinetics of NiAl. Although lower volume fraction is predicted at 525 °C, the growth and coarsening rates are consistent with the experiments. The peak hardness at 525 °C (Fig. 4(c)) in this alloy is achieved a few hours after the equilibrium fraction is reached due to particle growth still occurring (Fig. 4(b)); the particles coarse and decrease the number density of intermetallics (Fig. 4(b)) in the overaging conditions. Figure 4(d) shows the hardness predictions and experimental measurements in θ–containing Fe-Ni-Mn steels; $D_g = 30$ μm was assumed as no PAG size values were reported. The model is able to reproduce experimental observations at 500 °C, indicating that the predicted strengthening of NiMn particles are consistent with experimental data, as well as in predicting the hardening mechanisms in maraging steels; the discrepancies in growth kinetics at 400 °C and 440 °C can be due to temperature variations in the interfacial energy or due to a different struc-

ture formed in the steel; however no information was provided on the initial martensitic structure. It is worth noting that the ageing conditions in (d) correspond to the conditions shown in Figures 2 and 3 for the reverted austenite kinetics in PH13-8Mo and FeNiMn steels, respectively. This shows that the models are successful in correlating variations in microstructure and hardness.

Figure 5 shows results in Lean7Mn, Lean10Mn and Lean12Mn, where Ni_2AlTi precipitates form. Figure 5(a) shows the size evolution of Ni_2AlTi for different Mn content, where it is confirmed that also Mn accelerates the growth of these particles, however a weaker effect is predicted. Nevertheless, it is predicted that coarsening occurs after 10 hours. Figures 5(b), (c) and (d) show the hardness variation in these steels at different temperatures. At 420 °C, it takes more than 100 hours to reach the peak hardness in all cases due to the slow kinetics. Similarly, at 460 °C Lean7Mn reaches the peak hardness after 100 hours, whereas Lean10Mn and Lean12Mn reached the peak hardness after ~ 50 and ~ 2 hours, respectively. However, the model underpredicts the hardness during underaging; these discrepancies can be due to the partial formation of NiMn, especially with higher Mn content, which can later transition to Ni_2AlTi [24], or due to the interdiffusion of additional elements to the intermetallic increasing the values of r during early stages of precipitation [25]. Nevertheless, the model describes the experimental trends in the peak hardness values and overaging. Figure 5(d) shows H_v at 500 °C, where the peak hardness is reached in all cases within 2–10 hours, due to the rapid diffusion kinetics at high temperatures. This is also consistent with the increased kinetics in austenite reversion in Lean10Mn and Lean12Mn shown in Figure 4. The model overpredicts (underpredicts) the experiments by 50 H_v during overaging (underaging), although it shows good agreement in the hardening (softening) rates; these discrepancies can be due to a lower volume fraction of Ni_2AlTi not being considered, or due to interdiffusion of additional elements. Figures 4 and 5 show complete microstructural description and its correlation with strength in Lean7Mn, Lean10Mn and Lean12Mn during heat treatment.

To illustrate Ti effects on precipitation strengthening, Figure 6 shows the evolution of Ni_3Ti in C300 and M350 for various ageing temperatures, where Ti content in the

former and latter are 0.75 and 1.9 wt%, respectively. Figure 6(a) and (b) show the mean radius and length evolution of Ni_3Ti, respectively (assuming an aspect ratio of 4.5), and 6(c) shows the phase fraction evolution in C300 with time; the equilibrium volume fraction obtained from Thermocalc in C300 was 0.036, whereas in M350 it was 0.089. Figure 6(d) shows the concomitant variations in hardness showing the effects of precipitation and solid solution hardening in M350. In all cases the correlations between the models and experiments show good results, except f_p at 440 °C and H_v at 480 °C, where slower η kinetics are reported. This can be due to variations in the interfacial energy with temperature. Ti contributions during underageing stem from solid solution hardening and transition to precipitation hardening when Ni_3Ti form at peak hardness and during overaging. It is interesting noting that these steels show apparent higher peak hardness than their Al–containing counterparts (PH13-8Mo) in spite of having lower volume fraction; this is due to their rod–shape morphology increasing the critical–resolved stress for dislocations to bypass the particles.

8 Discussion

A theoretical framework for prescribing microstructure and strength evolution in maraging steels has been proposed. It is based on describing the hierarchical structure of the martensitic matrix, including the density of dislocations, laths, and high–angle grain boundaries. This microstructural landscape allowed introducing evolution equations for lath–shaped austenite, as it mostly forms at the lath boundaries, restricting their growth within a martensite lath. The prescription of the dislocation density provided the number density for intermetallic particles nucleation, where classical theories for precipitation nucleation, growth and coarsening where employed to describe the mean particle size and volume fraction. These results were combined to describe the evolution of the room–temperature hardness due to precipitation hardening under various ageing conditions in Fe-Ni–, Fe-Mn– and Fe-Ni-Mn–based maraging steels. Precipitation parameters for each kind of intermetallic and reverted austenite were obtained from the literature and validated with experiments. These results show that the modelling methodology is able

to describe microstructure and hardness in several maraging steels when modifying their chemical composition. This allows us to assess the individual contribution of alloying elements typically included in commercial steels. Moreover, the predictions on reverted austenite formation can also help us to design steels and heat treatments for increasing the ductility.

The hardness in these steels accounts for contributions of the martensite (via dislocation density and grain boundary strengthening), solid solution and precipitation hardening. It is interesting exploring their variation during ageing; Figure 7 shows the contribution of each mechanism to H_v in (a) M350 and (b) PH13-8Mo when ageing at 540 °C and 575 °C, respectively. In M350, Ni_3Ti shows the greatest contribution close to peak hardness ($t > 18$ s) and during overaging up to 5 h, whereas solid solution (from Ni and Ti) contributes significantly to the Hardness during underageing ($t < 18$ s) and decreases by 50 H_v when Ni_3Ti forms; the strength of the martensite is constant as no dislocation recovery has been considered. Conversely in PH13-8Mo, the solid solution contribution is not significantly affected by NiAl formation, as Ni and Al have lower strengthening constants (Table 4); precipitation strengthening is highest between 100 s and up to 2 h, however decreasing at longer times. These results show that precipitation strengthening can be very high for a given ageing window, however decreasing significantly during overaging; strengthening from the matrix and solid solution are necessary to ensure high strength for wider ageing conditions.

8.1 Elemental optimisation: alloying contributions to strength

Results in the previous section showed how distinct intermetallics contribute to the total strength of commercial steels. However, it is also interesting to explore how the hardness changes when modifying the alloying content of each element. Figure 8(a) shows Al effects on Fe-4Ni-10Mn-1Mo-Al (wt%) when ageing at 450 °C and forming Ni_2AlMn; experimental results of two lean maraging steels with similar compositions are also shown (Table 1); LeanLAl contains 1 wt% of Ti, hence increasing the initial hardness by 50 H_v. $D_g = 30$ μm was considered. The model shows good agreement with the experimental observations, showing an increase of $\sim$ 200 H_v when the Al content increases from 0.15

to 2.5 wt%. This is due to the increase in the volume fraction of Ni_2AlMn increasing precipitation strengthening effects. Figure 8(b) shows the effects of Ti additions in the Fe-18Ni-3Mo-Ti (wt%) system aged at 500 °C; $f_{Ni3Ti,eq}$ are estimated to be 0.093, 0.063 and 0.03, when adding 0.74, 1.4 and 2 wt% of Ti, respectively. $D_g = 20$ μm was assumed. Experimental peak hardness are also shown in a number of 18Ni-Ti-Mo steels containing similar Ti and Mo additions [6]. The model results show good agreement with experimental trends. Moreover, the increase in hardness when increasing Ti content is more pronounced than Al. This is illustrated by comparing Figures 8 (a) and (b), where the hardness in the Fe-18Ni-3Mo-Ti system increases up to 650 H_v with Ti additions of 2 wt%, whereas for the Fe-4Ni-Mn-Al it only increases up to $\sim$ 500 H_v with Al additions of 2 wt%; however, higher Ni content is required to form Ni_3Ti. Figure 8(c) shows the effects of Mo in the Fe-18Ni-0.74Ti-Mo system, where the hardness increases from 470 to 525 H_v when adding up to 3 wt%; the Mo contribution is lower as it mostly remains in solid solution. Figure 8(d) shows the hardness evolution when increasing Cu content in the Fe-16Cr-4Ni-Cu system aged at 580 °C; experimental results in 17-4 SS (Fe-16.24Cr-3.94Ni-3.4 Cu wt%) are also shown for comparison, where Cu precipitates have the main strengthening contribution [27]; $D_g = 50$ μm was estimated from [26]. The model shows an increase in hardness up to 475 H_v when adding 6 wt% of Cu, showing significantly lower strengthening than in previous cases; this is due to the increase in the volume fraction of Cu particles with Cu additions is lower (1 at% of copper is equivalent to 1% volume fraction). These results demonstrate that Ni_3Ti induce the highest strengthening effect, followed by NiAl and variants, and Cu clusters display the weakest effect.

Figure 9 shows the strengthening effects of multiple precipitation in the Fe-Mn-Ni-Al-Cu system when modifying alloying content [7]; the compositions and denominations are given in Table 1 (Mar6, Mar7, Mar9, Mar11 and Mar13). Ni_2AlMn and BCC-Cu are present in this system when ageing at 550 °C, and the coarsening rate in the latter is reduced by the presence of Ni_2AlMn. Hence, the interfacial energy in Ni_2AlMn is reduced to that for BCC-Cu (0.02 J/m^2) to account for combined growth kinetics. Figure 9(a) shows the hardness predictions when increasing the concentration of alloying elements

and their comparison with experimental data when ageing for 2 hours; the model shows good agreement with the experimental trends, where the peak hardness is achieved within the first hour [7], and H_v increases as the volume fraction of both precipitates increases. To illustrate their relative contribution, Figures 9(b) and (c) show the particle radius and number density increments in Mar11, respectively, showing good results in the growth and coarsening rates; although a higher number density is predicted, the variation in N_p for both kind of precipitates is well described; the discrepancies can be due to a lower dislocation density induced by lower alloying concentrations, or lower elemental partitioning effects. Figure 9(d) shows the individual contribution of Ni_2AlMn and BCC-Cu to the hardness in Mar11 (σ_{ss} and σ_{Mart} are also added to each prediction); Ni_2AlMn particles have higher strengthening than BCC-Cu; the peak hardness in Cu occurs $\sim$2 hours later than in Ni_2AlMn, although this is not observed in the total hardness; this is due to σ_p predicting an average evolution ($\sqrt{\sigma^2_{Ni2AlMn} + \sigma^2_{Cu}}$).

8.2 Elemental optimisation: ductility VS strength

An interesting aspect of this work is to correlate the strength/ductility tradeoff with alloying content and ageing time. For instance, in PH13-8Mo the peak hardness when ageing 525 and 575 °C is achieved between 2–10 hours (Fig.4(c)), whereas full transformation of austenite is achieved after 70 hours (Fig. 2(b)); the hardness then decreases to 300 H_v. Nevertheless, Schnitzer *et al.* [14] reported an increase in the total elongation from 11% (as–quenched) up to 20 % after the austenite forms. Similar results have been reported in other steels [15,25]. Thus, there is an apparent link between γ increase and elongation. To further support this, a number of experimental observations linking the volume fraction of reverted austenite and total elongation (El) in overaging conditions are shown in Figure 10(a). These data cover different Ni and Mn contents and ageing temperatures; they were obtained from [14, 25, 26, 84–86]. It is interesting noting that when $f_\gamma = 0$ (and when no grain–boundary embrittlement occurs), the elongation lies within 7-10 %, and it increases as f_γ increases. It is worth noting that this correlation does not rule out the fact that other mechanisms can control ductility in these steels, such as dislocation evolution in the martensite, precipitation structure and grain boundary processes. Nevertheless, the aim

of this section is to correlate microstructure evolution (reverted austenite) with ductility, based on experimental information collected in Figure 10(a), which covers mainly over-aging conditions and grain boundary embrittlement is not expected to operate. Since a description of the ductility in these steels is complex and it lies beyond the scope of the models, a linear relationship is adopted to quantitatively describe the trends observed: $El = 7 + 0.57 f_\gamma$, where f_γ is in %; these predictions are also shown in the figure. To illustrate how different additions of Ni and Mn can affect the total elongation, Figure 10(b) shows a contour plot of the γ equilibrium volume fraction in the Fe–Ni–Mn system for different Ni and Mn contents at 550 °C; the contour lines denote $f_{\gamma,eq}$ (in %) and these values were obtained from Thermocalc. Lower Mn additions than Ni are required to increase the equilibrium fraction, however the ageing time can affect the values of γ. Using the relationship obtained in (a), the increase in ductility with f_γ can be correlated with Ni and Mn content in the steel for a given ageing time. Figure 10(c) shows a contour plot of El (in %) for different Ni and Mn additions when ageing at 550 °C for 100 hours. It is observed that as $f_{eq,\gamma}$ increases, the time to reach the equilibrium volume fraction can increase, but this depends on the Ni and Mn content in the steel. For instance, in Figure 10(c), Fe-10Ni-2Mn and Fe-3Ni-6Mn have approximately the same elongation (20 %) and reverted austenite fraction ($\approx$ 23 %); however, the γ equilibrium fraction in the former and latter is $\approx$ 32 % and $\approx$ 25 %, respectively; this shows that after 100 hours, the reverted austenite in Fe-3Ni-6Mn is closer to equilibrium than in Fe-10Ni-2Mn, displaying faster kinetics. This map allows us defining an alloy design criterion to increase ductility in terms of Ni and Mn content; for instance, if $El \approx 15$ % is required, the combined Ni and Mn content in (c) should approximately be $1.6x_{Mn} + x_{Ni} \geq 8$ at%; a dashed line is highlighted in Figure 10(c) to show the lower limit of this region. Similar calculations can be done under different ageing conditions.

It also is possible to assess the strength/ductility tradeoff during overageing for alloy design strategies. Figure 10(d) shows the yield stress and ductility variations during overaging in M350, PH13-8Mo and 17-4SS, for different ageing times up to 500 hours at 550°C; Additionally, a variant of M350 containing 4 wt% of Mn and only 14.9 wt% of Ni

is shown with the remaining alloying additions being held constant; the fraction of Ni_3Ti decreases to 3.5 % in this case. These lines are obtained by estimating the variations in σ_Y when $f_\gamma > 0$ and using previous formula for the total elongation. $D_g = 20$ μm is assumed in all cases, whereas the parameters for γ are taken from the previous section. It is clearly seen how the strength drops drastically once the reverted austenite forms in all cases, *i.e.* when the elongation increases; M350 is the only alloy with yield strength above 1200 MPa to reach total elongation of 20 %. 17-4 SS is the weakest alloy, as it contains Cu particles and the low Ni content decreases the fraction of reverted austenite, therefore having the lower yield stress and elongation, and requiring longer times to reach peak hardness; the conventional inverse strength–elongation relationship does not hold for all ageing times, as the time to form BCC-Cu precipitates is of the same order of magnitude than the time when the reverted austenite forms at this temperature, hence a small increment in elongation and hardness is predicted, however no experimental validation was possible. It is interesting noting that the modified M350 does not change the variation between the strength and elongation, however the strength decreases by $\sim$ 100 MPa due to the lower intermetallic volume fraction. This alloy represents a good alternative to replace M350 at a lower cost if the strength and ductility required are 1200 MPa and greater than 20 %, respectively, displaying similar strength/elongation relationship than PH13-8Mo. However, it can be stronger by 150 MPa.

9 Conclusions

The following concluding remarks are summarised:

- A physics–based modelling framework for the microstructure and mechanical properties in maraging steels has been introduced. A critical assessment of typical alloying elements controlling the hardness and total elongation was performed.

- Descriptions for the lath–shaped reverted austenite and intermetallics were possible due to the characterisation of the hierarchical structure of the martensitic matrix. This includes prescribing the dislocation density, lath and high–angle boundary size.

- Reverted austenite kinetics promoted by Ni and Mn additions were described using

grain–boundary diffusion laws within a lath unit. Mn had stronger effect than Ni on increasing the growth rate and volume fraction.

- Descriptions for particle nucleation, growth, coarsening and volume fraction evolution were identified for Ni_3Ti, NiAl and its variants, and BCC–Cu clusters. The dislocation density provided the preferential nucleation sites for precipitation.

- Ti additions have the highest strengthening effect by precipitating Ni_3Ti; however high Ni content is required. Al additions also contribute to the strength without the need to increase Ni content by forming B2 and $L2_1$ intermetallics. Cu has the lower strengthening contribution due to the lower fraction of Cu clusters.

- A relationship between the reverted austenite and the total elongation in overaging conditions was found. This result not only allowed comparing the relative strength of different steels but also their ductility. Thus, a complete modelling suite for alloy design based on microstructure description was postulated.

Acknowledgements

This research was supported by the grant EP/L025213/1 from the UK Engineering and Physical Sciences Research Council (EPSRC). E.I. Galindo-Nava and P.E.J. Rivera-Díaz-del-Castillo are grateful to Prof. Mark Blamire for the provision of laboratory facilities.

References

[1] S. Nedjad, M. Ahmadabad, T. Furuhara, Correlation between the inter granular brittleness and precipitation reactions during isothermal aging of and Fe-Ni-Mn maraging steel, Mater Sci Eng A 490 (2008) 105–112.

[2] N. Heo, Ductile-brittle-ductile transition and grain boundary segregation of Mn and Ni in an Fe-6Mn-12Ni alloy, Scripta Mater 34 (1996) 1517–1522.

[3] H. Leitner, M. Schober, R. Schnitzer, S. Zinner, Strengthening behavior of Fe-Cr-Ni-Al-(Ti) maraging steels, Mater Sci Eng A 528 (2011) 5264–5270.

[4] D. Raabe, D. Ponge, O. Dmitrieva, B. Sander, Designing ultrahigh strength steels with good ductility by combining transformation induced plasticity and martensite aging, Adv Eng Mater 11 (2009) 547–555.

[5] V. Kardonskii, M. Perkas, High-strength maraging steel with a reduced cobalt concentration, Metallovedenie i Termicheskaya Obrabotka Metallov 6 (1968) 32–35.

[6] M. Rao, Progress in understanding the metallurgy of 18 % nickel maraging steels, Int J Mater Res 97 (2006) 1594–1607.

[7] M. Kapoor, D. Isheim, G. Ghosh, S. Vaynman, M. Fine, Y. Chung, Aging characteristics and mechanical properties of 1600 MPa body-centered cubic Cu and B2-NiAl precipitation-strengthened ferritic steel, Acta Mater 73 (2014) 56–74.

[8] Z. Guo, W. Sha, E. Wilson, Modeling the evolution of microstructure during the processing of maraging steels, JOM 56 (2004) 62–66.

[9] W. Xu, P. Rivera-Díaz-del-Castillo, S. van der Zwaag, Computational design of UHS maraging stainless steels incorporating composition as well as austenitisation and ageing temperatures as optimisation parameters, Phil Mag 89 (2009) 1647–1661.

[10] Q. Lu, W. Xu, S. van der Zwaag, A strain-based computational design of creep-resistant steels, Acta Mater 64 (2014) 133–143.

[11] R. Schnitzer, R. Radis, M. Nöhrer, M. Schober, R. Hochfellner, S. Zinner, E. Povoden-Karadeniz, E. Kozeschnik, H. Leitner, Reverted austenite in PH 13-8 Mo maraging steels, Mater Chem Phys 122 (2010) 138–145.

[12] S. Rajasekhara, P. Ferreira, Martensite $\rightarrow$ austenite phase transformation kinetics in an ultrafine-grained metastable austenitic stainless steel, Acta Mater 59 (2011) 738–748.

[13] H. Mirzadeh, A. Najafizadeh, Modeling the reversion of martensite in the cold worked AISI 304 stainless steel by artificial neural networks, Mater Design 30 (2009) 570–573.

[14] R. Schnitzer, G. Zickler, E. LAch, H. Clemens, S. Zinner, T. Lippmann, H. Leitner, Influence of reverted austenite on static and dynamic mechanical properties of a PH 13-8 Mo maraging steel, Mater Sci Eng A 527 (2010) 2065–2070.

[15] D. Squires, E. Wilson, Aging and brittleness in an Fe-Ni-Mn alloy, Metall Trans 3 (1972) 575–581.

[16] Y. Heo, M. Kim, H. Lee, Transformation of ordered face-centered tetragonal θ-MnNi phase to face-centered cubic austenite during isothermal ageing of an Fe-Mn-Ni alloy, Acta Mater 56 (2008) 1306–1314.

[17] E. Galindo-Nava, P. Rivera-Díaz-del-Castillo, A model for the microstructure behaviour and strength evolution in lath martensite, Acta Mater 98 (2015) 81–83.

[18] E. Galindo-Nava, P. Rivera-Díaz-del-Castillo, Understanding the factors controlling the hardness in martensitic steels, Scripta Mater 110 (2016) 96–100.

[19] R. Schnitzer, M. Schober, S. Zinner, H. Leitner, Effect of Cu on the evolution of precipitation in an Fe-Cr-Ni-Al-Ti maraging steel, Acta Mater 58 (2010) 3733–3741.

[20] F. Zhu, Y. Yin, R. Faulkner, Microstructural control of maraging steel C300, Mater Sci Tech 27 (2011) 395–405.

[21] Y. He, K. Yang, W. Sha, Microstructure and mechanical properties of a 2000 MPa grade Co-free maraging steel, Metall Mater Trans A 36 (2005) 2273–2287.

[22] J. Hu, L. Du, G. Sun, H. Xie, R. Misra, The determining role of reversed austenite in enhancing toughness of a novel ultra-low carbon medium manganese high strength steel, Scripta Mater 104 (1975) 87–90.

[23] J. Millán, S. Sandöbest, A. Al-Zubi, T. Hickel, P. Choi, J. Neugebauer, D. Ponge, D. Raabe, Designing hustler nanoprecipitates by elastic misfit stabilisation in Fe-Mn maraging steels, Acta Mater 76 (2014) 94–105.

[24] Y. Heo, H. Lee, Precipitation and fracture behaviour of Fe-Mn-Ni-Al alloys, Phil Mag 93 (2013) 4519–4531.

[25] F. Qian, Microstructural evolution of Mn–based maraging steels and their influences on mechanical properties, Ph.D. thesis, The University of Sheffield (2015).

[26] R. Bhambroo, S. Roychowdhury, K. Vivekanand, V. Raja, Effect of reverted austenite on mechanical properties of precipitation hardenable 17-4 stainless steel, Mater Sci Eng A 568 (2013) 127–133.

[27] U. Viswanathan, P. Nayar, R. Krishnan, Kinetics of precipitation in 17-4 PH stainless steel, Mater Sci Tech 5 (1989) 346–349.

[28] C. Kinney, K. Pytlewski, A. Khachaturyan, J. Morris Jr., The microstructure of lath martensite in quenched 9Ni steel, Acta Mater 69 (2014) 372.

[29] S. Morito, Y. Adachi, T. Ohba, Morphology and crystallography of sub-blocks in ultra-low carbon lath martensite steel', Mater Trans 50 (2009) 1919.

[30] S. Zhang, S. Morito, Komizo, Y, Variant selection of low carbon high alloy steel in an austenite grain during martensite transformation, ISJ 52 (2012) 510.

[31] G. Oslon, M. Cohen, A general mechanism of martensitic nucleation: Part I. General concepts and the FCC-HCP transformation, Metall Trans A 7 (1976) 1897.

[32] G. E. Dieter, Mechanical Metallurgy, McGraw Hill, 1988.

[33] G. Stibitz, Phys Rev 49 (1936) 859.

[34] H. Bhadeshia, R. Honeycombe, Steels: Microstructure and properties, Butterworth-Heinemann, 2006.

[35] J. Wilde, A. Cerezo, G. Smith, Three-dimensional atomic-scale mapping of a cottrell atmosphere around a dislocation in iron', Scripta Mater 43 (2000) 39.

[36] M. Kuzmina, M. Herbig, D. Ponge, S. Sandlöbes, D. Raabe, Linear complexions: confined chemical and structural states at dislocations, Science 349 (2015) 1080–1083.

[37] M. Miller, P. Pareige, Atomic level characterization of neutron irradiated pressure vessel steels, Mat Res Soc Symp 650 (2000) 1–12.

[38] O. Dmitrieva, D. Ponge, G. Inden, J. Millán, P. Choi, J. Sietsma, D. Raabe, Chemical gradients across phase boundaries between martensite and austenite in steel studied by atom probe tomography and simulation, Acta Mater 59 (2011) 364–374.

[39] U. Viswanathan, G. DEy, V. Sethumadhavan, Effects of austenite reversion during overageing on the mechanical properties of 18 Ni (350) maraging steel, Mater Sci Eng A 398 (2005) 367–372.

[40] K. Macek, P. Lukáš, J. Janovec, P. Mikula, P. Strunz, M. Vrána, M. Zaffagnini, Austenite content and dislocation density in electron-beam welds of a stainless maraging steel, Mater Sci Eng A 208 (1996) 131–138.

[41] K. Tomimura, S. Takaki, Y. Tokunaga, Reversion mechanism from deformation induced martensite to austenite in metastable austenitic stainless steels, ISIJ Int 12 (1991) 1431–1437.

[42] F. Mossier, E. Povoden-Karadeniz, S. Pogatscher, P. Uggowitzer, Y. Estrin, S. Gerstl, E. Kozeschnik, J. Löfeller, Reverse $\alpha' \rightarrow \gamma$ transformation mechanisms of martensitic Fe-Mn and age-hardenable Fe-Mn-Pd alloys upon fast and slow continuous heating, Acta Mater 72 (2014) 99–109.

[43] F. Humphreys, M. Hatherly, Recrystallization and related annealing phenomena, Elsevier, 2004.

[44] E. Kozeschnik, Modeling solid-state precipitation, Momentum press, 2013.

[45] R. Tewari, S. Mazumdea, I. Batra, G. Dey, S. Banerkee, Precipitation in 18 wt% Ni maraging steel of grade 350, Acta Mater 48 (2000) 1187–1200.

[46] M. Hättestrand, J. Nilsson, K. Stiller, P. Liu, M. Andersson, Precipitation hardening in a 12%Cr-9%Ni-4%Mo-2%Cu stainless steel, Acta Mater 52 (2004) 1023–1037.

[47] J. Svoboda, F. Fischer, P. Fratzl, E. Kozeschnik, Modeling of kinetics in multicomponent multi-phase systems with spherical precipitates I: Theory, Mater Sci Eng A 385 (2004) 166–174.

[48] I. Loginova, J. Odqvist, G. Amberg, J. Agren, The phase-field approach and solute drag modelling of the transition to massive $\gamma \rightarrow \alpha$ transformation in binary Fe-C alloys, Acta Mater 51 (2003) 1327–1339.

[49] A. Yamanaka, T. Takaki, Y. Tomita, Phase-field simulation of austenite to ferrite transformation and Widmanstäthen ferrite formation in Fe-C alloy, Mater Trans 47 (2006) 2725–2731.

[50] W. Lange, M. Enomoto, H. Aronson, The kinetics of ferrite nucleation at austenite grain boundaries in Fe-C alloys, Metall Trans A 19 (1988) 427–440.

[51] J. Pardal, S. Tavares, M. Cindra Fonseca, Study of the austenite quantification by X-ray diffraction in the 18Ni-Co-Mo-Ti maraging 300 steel, J Mater Sci 31 (2006) 2301–2307.

[52] V. Vasudevan, S. Kim, C. Wayman, Precipitation reactions and strengthening behavior in 18 wt pct nickel maraging steels, Metall Trans A 21 (1990) 2655–2668.

[53] M. Schober, R. Schnitzer, H. Leitner, Precipitation evolution in a Ti-free and Ti-containing stainless maraging steel, Ultramicroscopy 109 (2009) 553–562.

[54] J. Millán, D. Ponge, D. Raabe, P. Choi, O. Dmitrieva, Characterisation of nano-sized precipitates in a Mn-based lean maraging steel by atom probe tomography, Steel research Int 82 (2011) 137–145.

[55] Y. He, K. Yang, W. Qu, F. Kong, G. Su, Effects of solution treatment temperature on grain growth and mechanical properties of high strength 18% Ni cobalt free maraging steel, Mater Sci Tech 19 (2003) 117–124.

[56] W. Sha, Z. Guo, Maraging steels: modelling of microstructure, properties and applications, Woodhead Publishing, 2009.

[57] S. Kim, C. Wayman, Precipitation behaviour and microstructural changes in maraging Fe-Ni-Mn-Ti alloys', Mater Sci Eng A 128 (1990) 217–230.

[58] H. Leitner, M. Schober, R. Schnitzer, Splitting phenomenon in the precipitation evolution in an Fe-Ni-Al-Ti-Cr stainless steel, Acta Mater 58 (2010) 1261–1269.

[59] S. Goodman, S. Brenner, J. Low, An FIM-Atom probe study of the precipitation of copper from iron-1.4 at. pct copper, Metall Trans A 4 (1973) 2363–2369.

[60] M. Perez, D. Dumont, D. Acevedo-Reyes, Implementation of classical nucleation and growth theories for precipitation, Acta Mater 56 (2008) 2119–2132.

[61] M. Perrier, A. Deschamps, O. Bouaziz, Y. Brechet, F. Danoix, F. De Geuser, P. Donnadieu, K. Hoummada, P. Maugis, Characterisation and modeling of precipitation kinetics in a Fe-Si-Ti alloy, Metall Mater Trans A 43 (2012) 4999–5008.

[62] M. Bonvalet, T. Philippe, X. Sauvage, D. Blavette, Modeling of precipitation kinetics in multicomponent systems: Application to model superalloys, Acta Mater 100 (2015) 169–177.

[63] L. Rougher, A. Jacot, C. Gandin, P. Di Napoli, P. Thývery, D. Ponsen, V. Jaquet, Numerical simulation of precipitation in multicomponent Ni-base alloys, Acta Mater 61 (2013) 6396–6405.

[64] S. Yamasaki, H. Bhadeshia, Modelling and characterisation of Mo_2C precipitation and cementite dissolution during tempering of Fe-C-Mo martensitic steel, Mater Sci Tech 19 (2003) 723–731.

[65] G. Stechauner, E. Kozeschnik, Thermo-kinetic modelling of Cu precipitation in α-Fe, Acta Mater 100 (2015) 135–146.

[66] M. Perez, Gibbs-Thomson effects in phase transformations, Scripta Mater 52 (2005) 709–712.

[67] Z. Teng, M. Miller, G. Ghosh, C. Liu, S. Huang, K. Russell, M. Fine, P. Liaw, Characterisation of nanoscale NiAl-type precipitates in a ferritic steel by electron microscopy and atom probe tomography, Scripta Mater 63 (2010) 61–64.

[68] C. Liebscher, V. Radmilovic, U. Dahmen, M. Asta, G. Ghosh, On the formation of hierarchically structured $L2_1$-Ni_2TiAl type precipitates in a ferritic alloy, J Mater Sci 48 (2013) 2067–2075.

[69] J. Robson, H. Bhadeshia, Modelling precipitation sequences in power plant steels. Part 1 - kinetic theory, Mater Sci Tech 13 (1997) 631–639.

[70] A. Deschamps, Y. Brechet, Influence of pre deformation and ageing of an Al-Zn-Mg alloy-II. Modeling of precipitation kinetics and yield stress, Acta Mater 47 (1999) 293–305.

[71] Y. Heo, M. Takeuchi, K. Furuya, H. Lee, Transformation of DO_{24} η-Ni_3Ti phase to face-centered cubic austenite during isothermal aging of an Fe-Ni-Ti alloy, Acta Mater 57 (2009) 1176–1187.

[72] H. Calderon, M. Fine, Coarsening kinetics of coherent NiAl-type precipitates in Fe-Ni-Al and Fe-Ni-Al-Mo alloys, Mater Sci Eng 63 (1984) 197–208.

[73] I. Holzer, E. Kozeschnik, Computer simulation of the yield strength evolution in Cu-precipitation strengthened ferritic steel, Mater Sci Eng A 527 (2010) 3546–3551.

[74] E. Pereloma, D. Edmonds, Phase transformations in steels: Diffusionless transformations, High Strength Steels, Modelling and Advanced Analytical Techniques, Elsevier, 2012.

[75] D. Lide, CRC Handbook of Chemistry and Physics, CRC Press, 2008.

[76] S. Morito, H. Yoshida, T. Maki, X. Huang, Effect of block size on the strength of lath martensite in low carbon steels', Mater Sci Eng A 438 (2006) 237.

[77] R. Schnitzer, S. Zinner, H. Leitner, Modeling of the yield strength of a stainless maraging steel, Scripta Mater 62 (289) 286.

[78] G. Ansell, F. Lenel, Criteria for yielding of dispersion-strengthened alloys, Acta Metall 8 (1960) 612–616.

[79] M. Green, G. Chin, J. Vander sand, Plastic deformation of single crystals of the heusler alloy Cu_2MnAl, Metall Trans A 8 (1977) 353–361.

[80] A. Ardell, Precipitation hardening, Metall Trans A 16 (1985) 2131–2165.

[81] R. Fleischer, Substitutional solution hardening, Acta Metall 11 (1963) 203.

[82] R. Labusch, A statistical theory of solid solution hardening, Phys Stat Sol 41 (1970) 659–669.

[83] M. Karimi, A. Najafizadeh, A. Kermanpur, M. Eskandari, Effect of martensite to austenite reversion on the formation of nano/submicron grained AISI 301 stainless steel, Mater Charac 60 (2009) 1220–1223.

[84] P. Gibbs, E. De Moor, M. Merwin, B. Clausen, J. Speer, D. Matlock, Austenite stability effects on tensile behavior of manganese- enriched-austenite transformation-induced plasticity steel, Metall Mater Trans A 42 (2011) 3691–3702.

[85] J. Han, S. Lee, J. Jung, Y. Lee, The effects of the initial martensite microstructure on the microstructure and tensile properties of intercritically annealed Fe-9Mn-0.05C steel, Acta Mater 78 (2014) 369–377.

[86] R. Miller, Ultrafine-grained microstructures and mechanical properties of alloy steels, Metall Trans 3 (1972) 905–912.

[87] D. Vanderwalker, The precipitation sequence of Ni_3Ti in Co-free maraging steel, Metall trans A 18 (1987) 1191–1194.

[88] K. Hirano, M. Cohen, B. Averbach, Diffusion of nickel into iron, Acta Metall 9 (1961) 440–445.

[89] W. Gale, T. Totemeier, Smithells Metals reference books, Butterworth-Heinemann, 2003.

[90] A. Bowen, G. Leak, Solute diffusion in alpha- and gamma-iron, Metall Trans 1 (1970) 1695–1700.

[91] M. Salamon, H. Mehrer, Interdiffusion, kirkendall effect, and Al self-diffusion in iron-aluminium alloys, Int J Mater Res 96 (2005) 4–16.

[92] V. Shapovalov, A. Kurasov, Diffusion of titanium into iron, Metallovedenie i Termicheskaya Obrabotka Metallov 9 (1975) 71–73.

[93] M. Anand, R. Agarwala, Diffusion of copper in iron, J App Phys 37 (1966) 4248.

Table 1: Chemical composition (in wt%) of the steels tested in this work.

Steel	Ni	Mn	Co	Cr	Al	Ti	Mo	Cu	C	Author
PH13-8Mo	8.2	-	-	12.7	1.1	-	2.2	-	0.03	[3, 14, 19]
C300	18.8	-	8.5	-	0.12	0.75	4.75	-	-	[20]
M350	18.9	-	0.22	-	0.05	1.9	4.1	-	0.0037	[21]
5Mn	0.3	5	-	-	0.01	-	0.2	-	0.04	[22]
Fe8Ni8Mn	8	8	-	-	-	-	-	-	-	[24]
Fe12Ni6Mn	12	6	-	-	-	-	-	-	0.006	[15]
LeanLAl	1.97	9.1	-	-	0.155	1	1	-	0.0056	[23]
LeanHAl	2.98	8.76	-	-	1.33	-	-	-	0.01	[23]
Lean7Mn	2	7	-	-	1	1	1	-	0.03	[25]
Lean10Mn	2	10	-	-	1	1	1	-	0.015	[25]
Lean12Mn	2	12	-	-	1	1	1	-	0.02	[25]
AISI 301	6.5	1.29	-	17.3	-	-	-	-	0.11	[83]
17-4 SS	3.94	0.52	-	16.24	-	-	-	3.3	0.049	[26]
Mar6	2.5	0.5	-	-	0.6	-	-	2.5	0.06	[7]
Mar7	2.5	1.5	-	-	0.5	-	-	2.5	0.06	[7]
Mar9	4	1.5	-	-	1	-	-	2.5	0.05	[7]
Mar11	4	3	-	-	1.5	-	-	3	0.05	[7]
Mar13	4	4	-	-	1	-	-	4	0.05	[7]

Table 2: Intermetallics usually observed in multicomponent maraging steels.

Intermetallic	Structure	Fe	Ni	Mn	Ti	Al	Mo	Cu	Morphology	Author
NiMn (θ)	$L1_0$	X	X	X	-	-	-	-	Lenticular	[15, 16, 23]
Ni_2AlMn	$L2_1$	X	X	X	-	X	-	-	Spherical	[16]
NiAl (β')	B2	X	X	-	-	X	X	-	Spherical	[53]
Ni_2AlTi	$L2_1$	X	X	X	X	X	X	-	Spherical	[25, 54]
Ni_3Ti (η)	$D0_{24}$	X	X	X	X	-	-	-	Rod	[52, 57, 87]
Ni_3(Ti,Al), NiAl	$D0_{24}$, B2	X	X	-	X	X	X	-	Rod (η), Spherical	[58]
Ni_3(Ti,Al), NiAl, Cu	$D0_{24}$, B2, BCC	X	X	-	X	X	X	X	Rod (η), Spherical	[19]
NiAl, Cu	B2, BCC	X	X	X	-	X	-	X	Spherical	[7]

Table 3: Diffusion parameters of the alloying elements for the steels tested in this work.

Element	Fe	Ni	Mn	Cr	Al	Ti	Cu
D_0 (m^2/s)	5×10^{-5}	1.4×10^{-4}	1.5×10^{-4}	8.5×10^{-4}	1.8×10^{-3}	2×10^{-3}	5.7×10^{-5}
Q (kJ/mol)	240	245.6	233	250.6	233	242.6	244
Ref.	[34]	[88]	[89]	[90]	[91]	[92]	[93]

Table 4: Solid solution strengthening constants.

Element	Ni	Mn	Cr	Al	Ti	Mo	Cu
β_i (MPa/at)	708	540	622	196	2628	2362	320

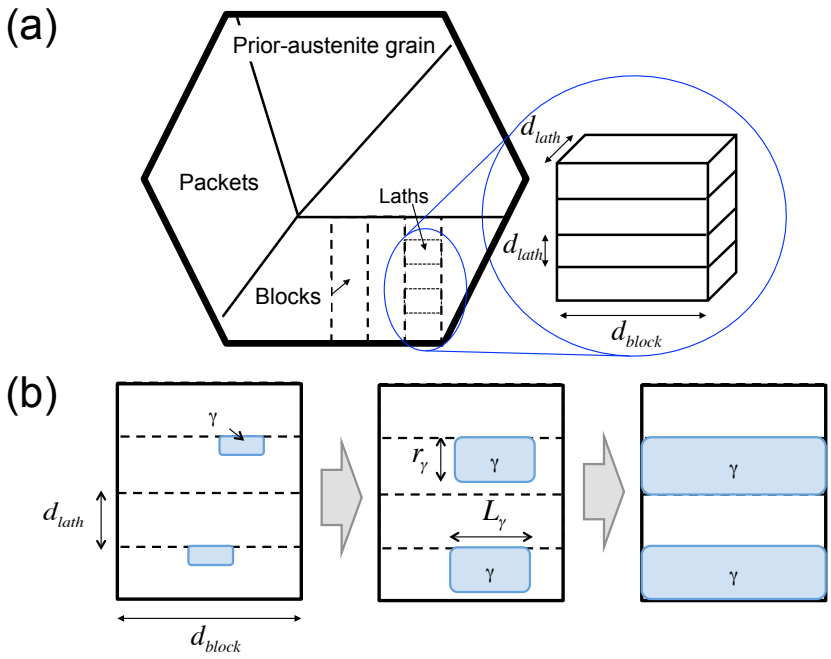

Figure 1: (a) Schematic representation of the hierarchical structure of lath martensite with laths of cuboidal morphology. (b) Mechanism of austenite reversion in lath martensite.

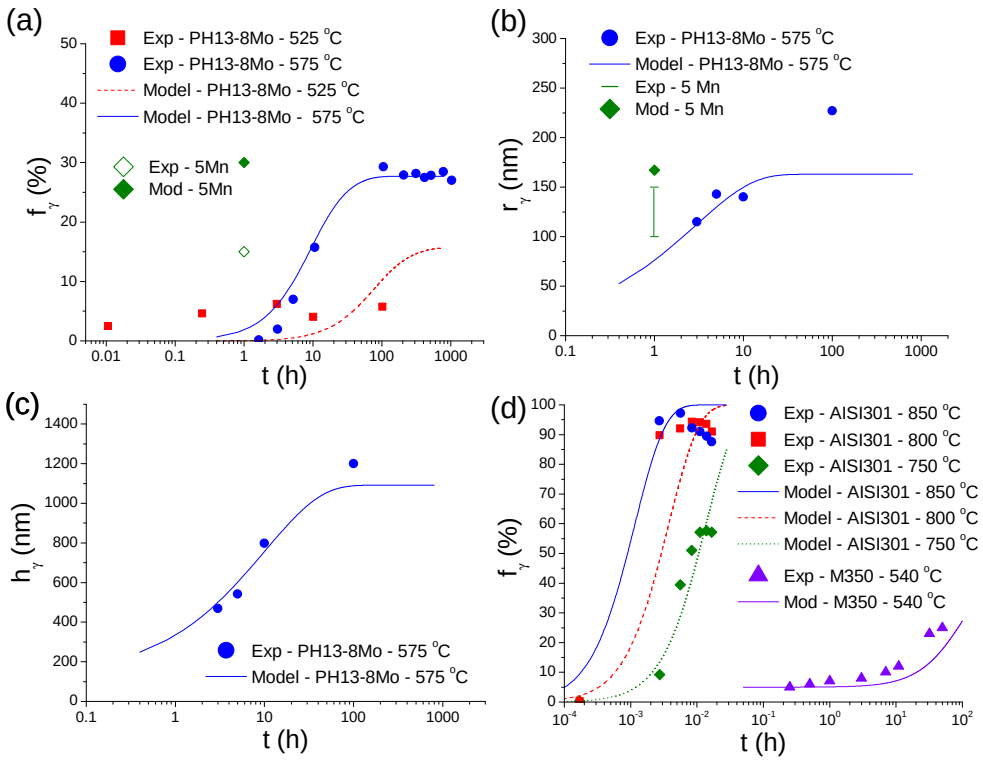

Figure 2: Reverted austenite predictions in PH13-8Mo and 5Mn, including (a) volume fraction, (b) lath thickness and (c) length. (d) $\alpha' \rightarrow \gamma$ transformation kinetics in AISI301 at high temperatures and reverted austenite evolution in Mart1.

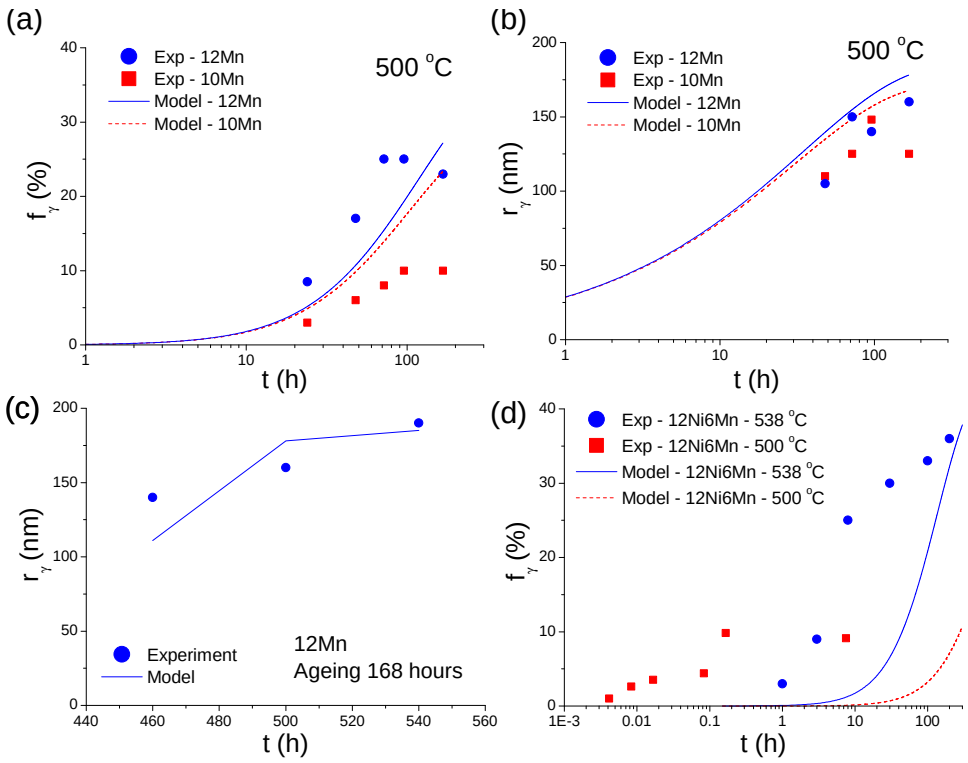

Figure 3: Reverted austenite evolution in Lean7Mn, Lean10Mn and Lean12Mn at different temperatures, including (a) volume fraction and (b) thickness; (c) r_γ evolution in Lean12Mn at various temperatures. (d) Effect of Mn in f_γ evolution in two maraging steels.

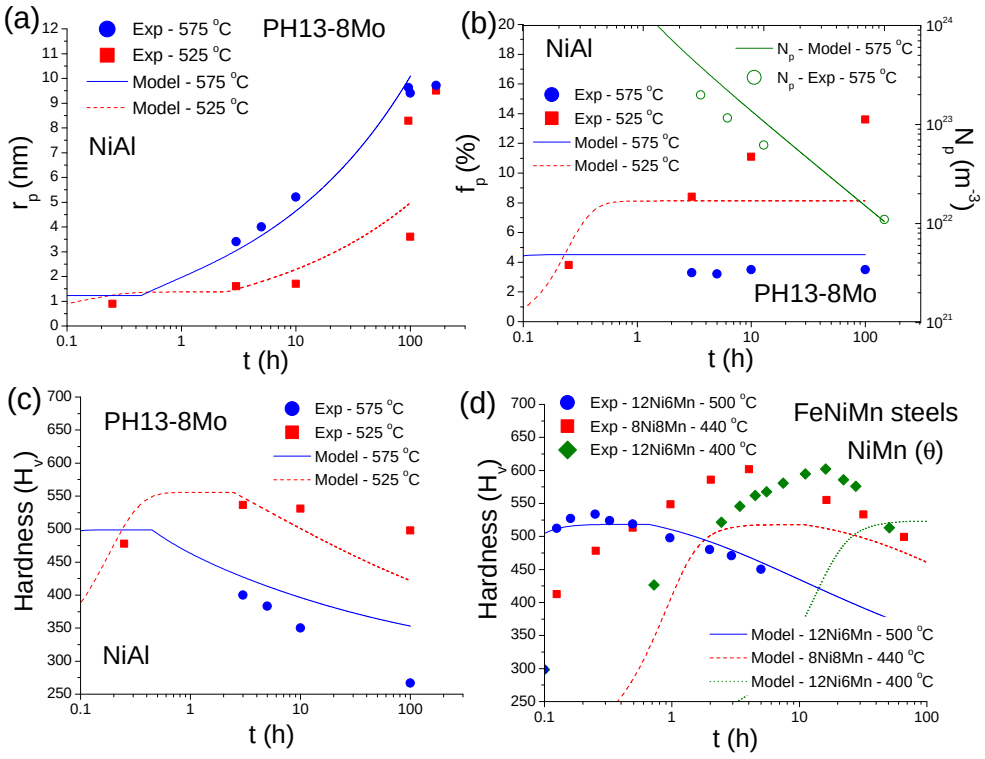

Figure 4: Results on intermetallic formation and strengthening in PH13-8Mo: (a) mean particle radius, (b) volume fraction and number density and (c) hardness evolution. (d) Hardness evolution in θ–containing Fe–Ni–Mn steels.

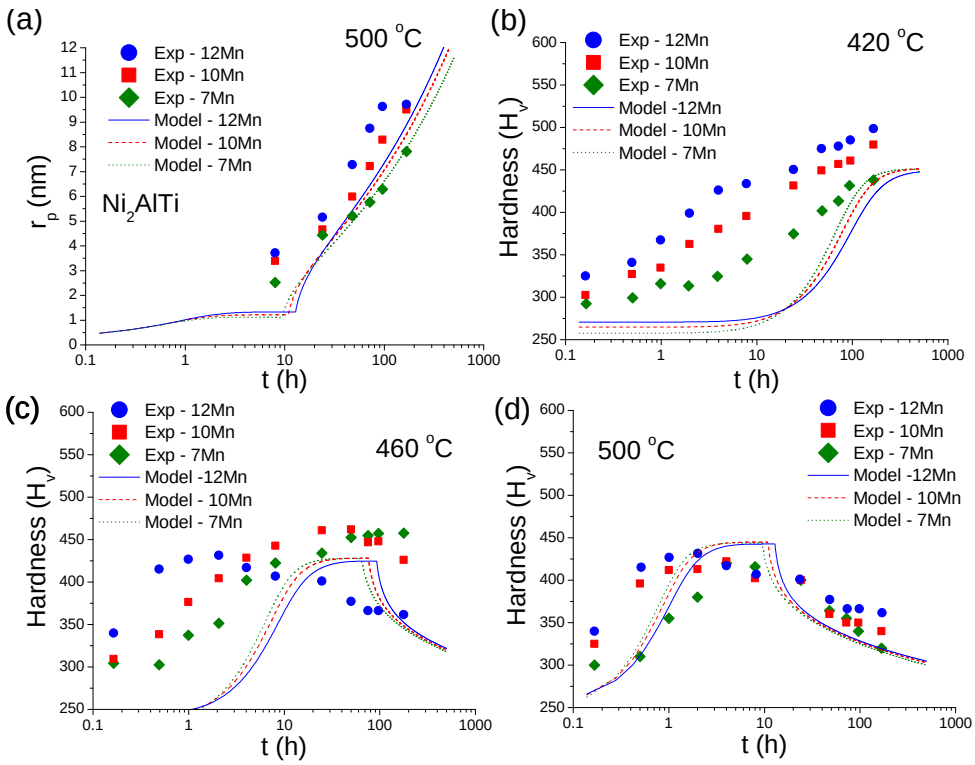

Figure 5: Results on intermetallic formation and strengthening in Lean7Mn, Lean10Mn and Lean12Mn. (a) particle radius, and hardness evolution at (b) 420 °C, (b) 460 °C, (b) 500 °C.

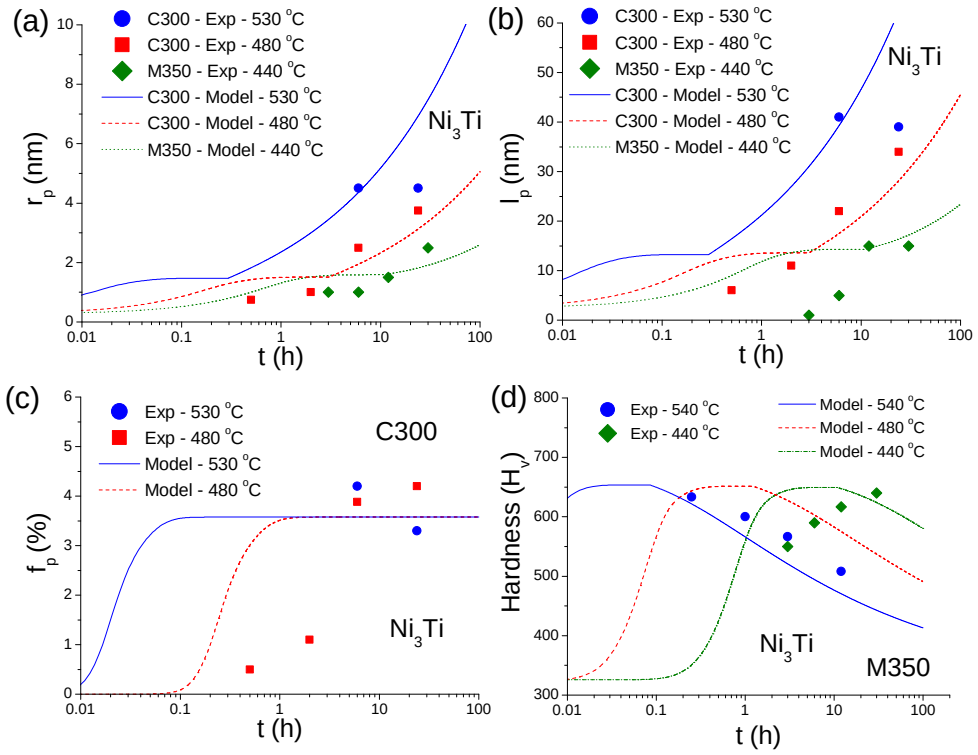

Figure 6: Results on Ni_3Ti formation and strengthening in C300 and M350: (a) particle radius and (b) length; (b) phase fraction evolution, and its (d) corresponding hardness.

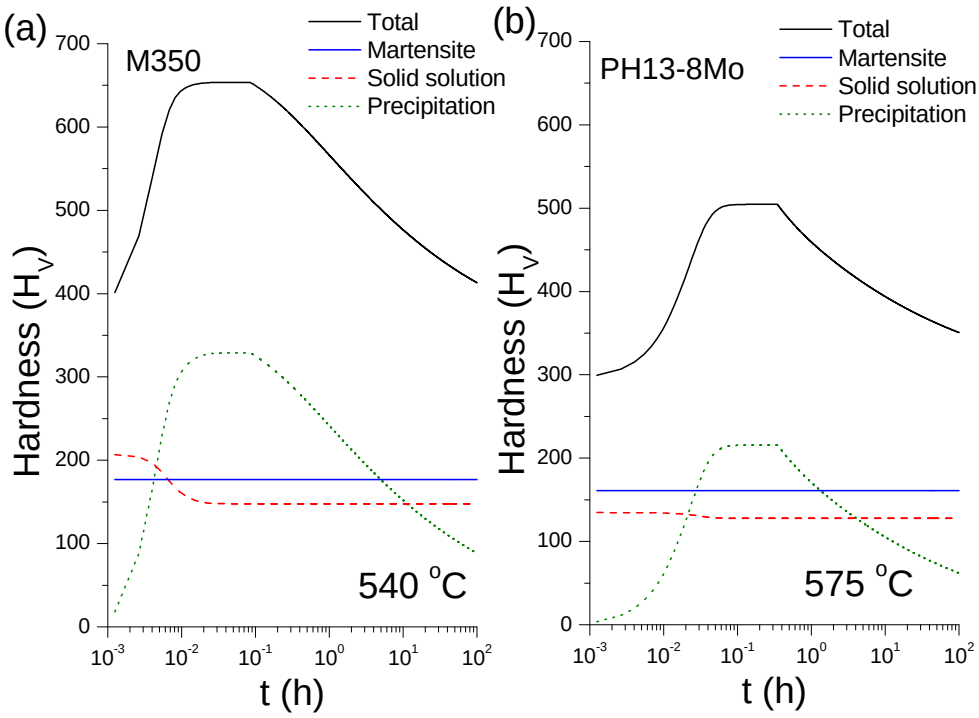

Figure 7: Relative contribution to strengthening in (a) M350 and (b) PH13-8Mo.

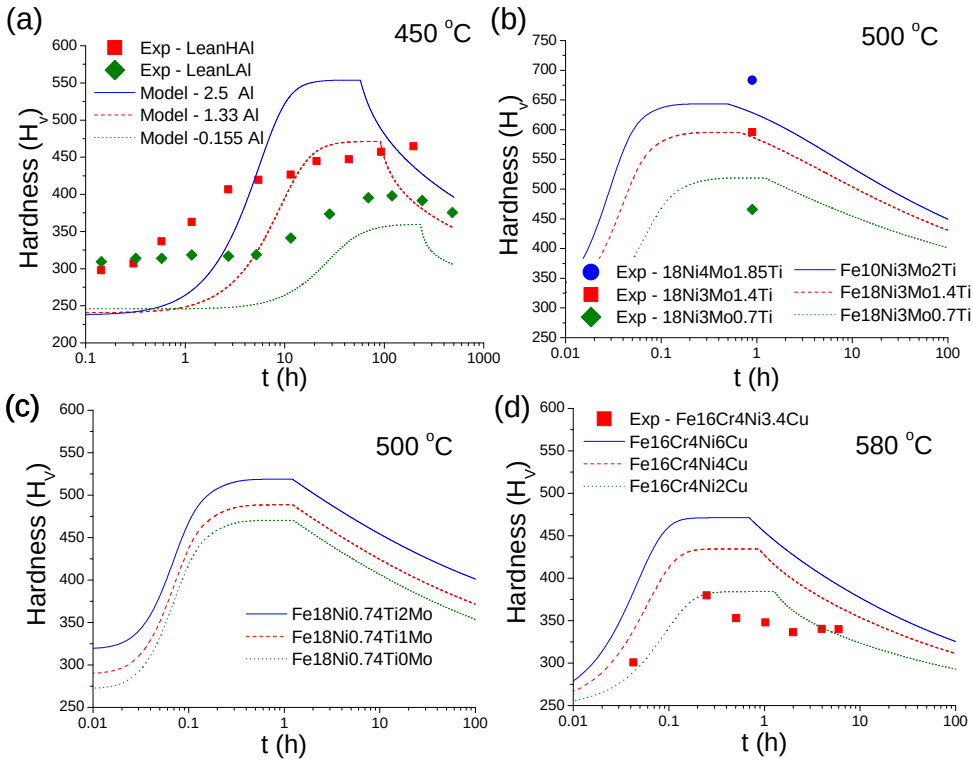

Figure 8: Analysis on the hardness variations with alloying content. (a) Al effects in Fe-2Ni-10Mn-1Mo-Al; (b) Ti effects in Fe-18Ni-3Mo-Ti; (c) Mo effects in Fe-18Ni-0.74Ti-Mo; and (d) Cu effects on Fe-16Cr-4Ni-Cu.

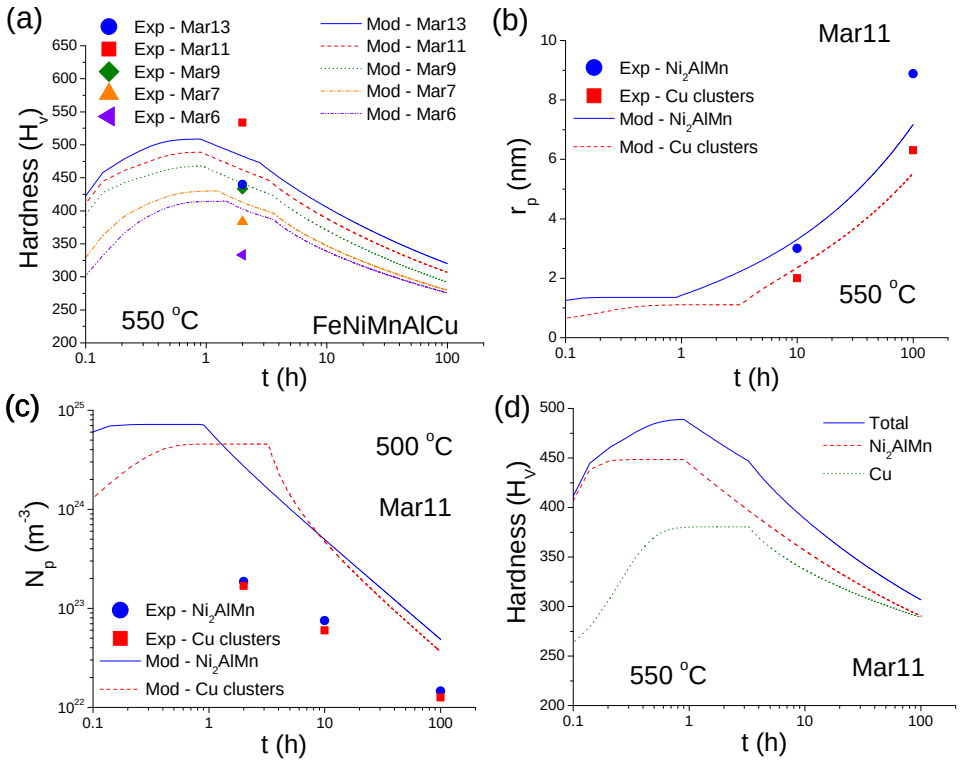

Figure 9: Strengthening analysis when multiple precipitation occurs in Fe-Mn-Ni-Al-Cu. (a) Variations in the hardness for various compositions; (b) mean particle radius and (c) number density in Mar11. (d) Individual strengthening contribution in Mar11 from Ni_2AlMn and Cu precipitates.

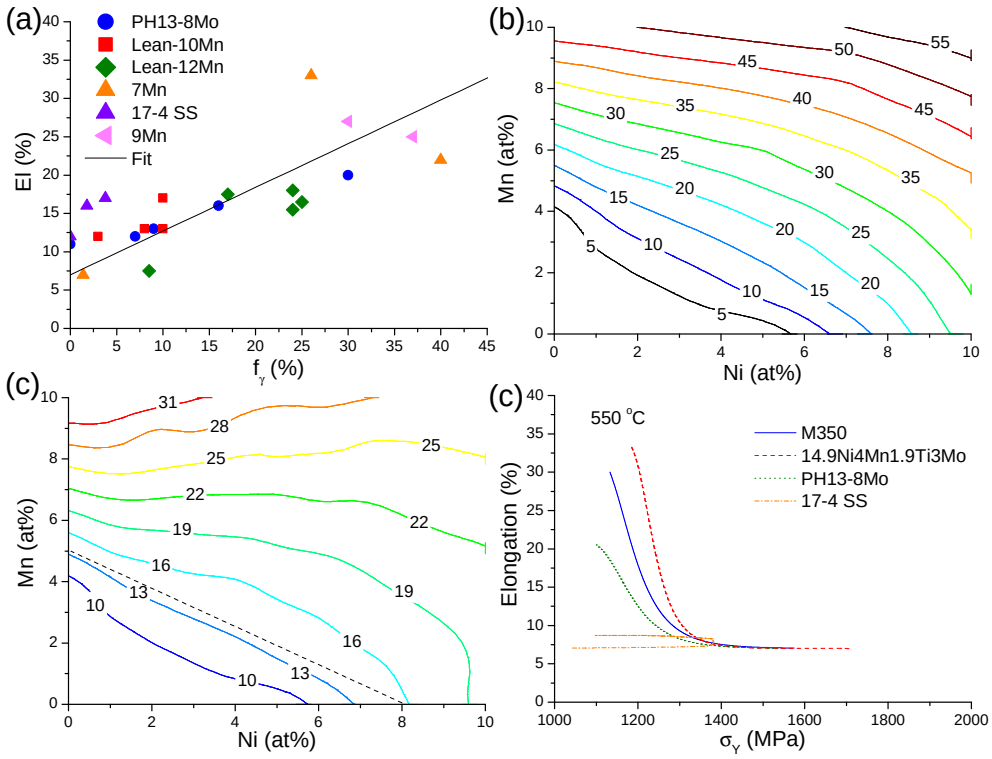

Figure 10: Elongation analysis in maraging steels: (a) Correlation between f_γ and total elongation. Contour plots of (b) γ equilibrium fraction at 550°C and (c) expected elongation for different Ni and Mn contents when ageing at 550°C for 100 hours. (d) Strength/ductility variations in various grades when ageing up to 500 hours.